POLITECNICO DI TORINO
Repository ISTITUZIONALE

Blast-induced liquefaction in silty sands for full-scale testing of ground improvement methods: Insights from a multidisciplinary study

(Article begins on next page)

19 April 2024

1 # Blast-induced liquefaction in silty sands for full-scale testing of ground improvement

2 ## methods: insights from a multidisciplinary study

3

4 Sara Amoroso[a, b], Kyle M. Rollins[c], Paul Andersen[c], Guido Gottardi[d], Laura Tonni[d], Maria F.

5 García Martínez[d], Kord Wissmann[e], Luca Minarelli[b], Cesare Comina[f], Daniela Fontana[g], Paolo

6 Marco De Martini[h], Paola Monaco[i], Arianna Pesci[j], Vincenzo Sapia[h], Maurizio Vassallo[b], Marco

7 Anzidei[h], Andrea Carpena[k], Francesca Cinti[h], Riccardo Civico[h], Igino Coco[h], Dario Conforti[l], Fawzi

8 Doumaz[h], Fabio Giannattasio[h], Giuseppe Di Giulio[b], Sebastiano Foti[m], Fabiana Loddo[j], Stefano

9 Lugli[g], Maria R. Manuel[n], Diego Marchetti[o], Mauro Mariotti[p], Valerio Materni[h], Brian Metcalfe[e],

10 Giuliano Milana[h], Daniela Pantosti[h], Antonio Pesce[f], Aura C. Salocchi[g], Alessandra Smedile[h],

11 Marco Stefani[q], Gabriele Tarabusi[j], Giordano Teza[r]

12

13 [a]*Department of Engineering and Geology, University of Chieti-Pescara, Viale Pindaro 42, 65129 Pescara, Italy*

14 [b]*Istituto Nazionale di Geofisica e Vulcanologia, viale Crispi 43, 67100 L'Aquila, Italy*

15 [c]*Department of Civil and Environmental Engineering, Brigham Young University, 430 Engineering Building, Provo,*

16 *Utah 84602, USA*

17 [d]*Department of Civil, Chemical, Environmental, and Materials Engineering, University of Bologna, Viale del*

18 *Risorgimento 2, 40136 Bologna, Italy*

19 [e]*Geopier Foundation Company, 130 Harbour Place Drive, Davidson, North Carolina 28036*

20 [f]*Department of Earth Sciences, University of Turin, via Valperga Caluso 35, 10125 Torino, Italy*

21 [g]*Department of Chemical and Geological Sciences, University of Modena and Reggio Emilia, via Campi 103, 41125*

22 *Modena, Italy*

23 [h]*Istituto Nazionale di Geofisica e Vulcanologia, via di Vigna Murata 605, 00143 Rome, Italy*

24 [i]*Department of Civil, Construction-Architectural and Environmental Engineering, University of L'Aquila, Piazzale*

25 *Ernesto Pontieri, Monteluco di Roio, 67100 L'Aquila, Italy*

26 [j]*Istituto Nazionale di Geofisica e Vulcanologia, via Donato Creti 12, 40128 Bologna, Italy*

27 [k]*Georeflex srl, via Carlo Fioruzzi 15, 29121 Piacenza, Italy*

28 [l]*Teledyne Optech Incorporated, 300 Interchange Way, Vaughan, Ontario, L4K 5Z8 Canada*

29   [m]*Department of of Structural, Building and Geotechnical Engineering, Politecnico di Torino, corso Duca degli Abruzzi*

30   *24, 10129 Turin, Italy*

31   [n]*GEO Geotecnica e Geognostica srl, Via Faucio 16, 03033 Arpino, Italy,*

32   [o]*Studio Prof. Marchetti srl, via Bracciano 38, 00189 Rome, Italy*

33   [p]*Sara Electronic Instruments srl, Via A. Mercuri 4, 06129 Perugia, Italy*

34   [q]*Department of Architecture, University of Ferrara, Via della Ghiara 36, 44121 Ferrara, Italy*

35   [r]*Department of Geosciences, University of Padua, via Gradenigo 6, 35131 Padua, Italy*

36

37   HIGHLIGHTS

38   Blast tests produced liquefaction and sand boils at a silty sand site in northern Italy

39   Blast tests produced volumetric strain similar to that expected in an earthquake

40   Aggregate piers as a liquefaction hazard mitigation strategy improved soil performance

41   Geophysical and geotechnical site investigations were carried out before and after blasting

42   Field responses of treated and non-treated soils during blasting were compared

43

44   ABSTRACT

45   In the engineering geology field increased attention has been posed in recent years to potential

46   liquefaction mitigation interventions in susceptible sand formations. In silty sands this is a major

47   challenge because, as the fines content increases, vibratory methods for densification become

48   progressively less effective. An alternative mitigation technique can be the installation of Rammed

49   Aggregate Pier® (RAP) columns that can increase the resistance of the soil, accounting for its

50   lateral stress increase and for the stiffness increase from soil and RAP composite response. To

51   investigate the influence of these factors on liquefaction resistance, full-scale blast tests were

52   performed at a silty sand site in Bondeno (Ferrara, Italy) where liquefaction was observed after the

53   2012 Emilia-Romagna earthquake. A multidisciplinary team of forty researchers carried out

54   devoted experimental activities aimed at better understanding the liquefaction process at the field

55   scale and the effectiveness of the treatment using inter-related methods. Both natural and improved

56 areas were investigated by in-situ tests and later subjected to controlled blasting. The blast tests

57 were monitored with geotechnical and geophysical instrumentation, topographical surveying and

58 geological analyses on the sand boils. Results showed the RAP effectiveness due to the

59 improvement of soil properties within the liquefiable layer and a consequent reduction of the blast-

60 induced liquefaction settlements, likely due to soil densification and increased lateral stress. The

61 applied multidisciplinary approach adopted for the study allowed better understanding of the

62 mechanism involved in the liquefaction mitigation intervention and provided a better overall

63 evaluation of mitigation effectiveness.

64

65 *Keywords*: liquefaction, blast test, rammed aggregate piers, ground improvement, silty sands,

66 Emilia-Romagna earthquake

67

68 **1. Introduction**

69 The identification of an effective soil improvement technique for the mitigation of liquefaction

70 hazard in silty sand deposits is undoubtedly a major challenge for engineers, geologists, building

71 owners, developers, and specialty contractors. Indeed, as the fines content increases, the normally

72 adopted vibratory methods for densification become progressively less effective and therefore more

73 expensive approaches, such as soil mixing or deep foundations, are often required. Most of these

74 alternative techniques are based on the installation of stiffer elements within the soil aimed at

75 increasing both strength and soil density: typical examples are the Rammed Aggregate Piers®

76 (RAP), Stone Columns (SC), Low Mobility Grout (LMG) or Timber Displacement Pile (TDP). In

77 recent years, the Resonant Compaction Method (RCM) has also been investigated as a ground

78 improvement solution in liquefaction-prone silts-silty sands (e.g. Li et al., 2018).

79 Over the last decades, a large amount of research has been carried out on liquefaction mitigation in

80 clean sands, especially with reference to ground improvement techniques by densification. In recent

81 years research interest has been also extended to liquefaction-prone deposits of silts and silty sands.

82 It is worth mentioning here the valuable outcomes from the extensive investigations carried out in

83 Christchurch (New Zealand), following the widespread liquefaction and lateral spreading evidences

84 due to the 2010-2011 Canterbury earthquake sequence (Giona Bucci et al., 2018). Wissmann et al.

85 (2015), Vautherin et al. (2017), and Amoroso et al. (2018) examined the performance of RAP

86 installation, showing that densification can be obtained and reliably quantified by means of

87 piezocone (CPTU) and flat dilatometer (DMT) measurements in granular soil deposits having a soil

88 behaviour type index I_c < 1.8 or a material index I_D > 1.8, also at depths exceeding the design

89 treatment depth. Wotherspoon et al. (2015) and Hwang et al. (2017) assessed the effectiveness of

90 soil stiffening caused by the installation of SC, RAP and LMG using cross-hole tests. RAP

91 appeared to produce stiffer discrete inclusions than SC, while LMG column installation actually

92 compromised the liquefaction resistance. Finally, Alexander et al. (2017) examined the performance

93 of a SC foundation system subjected to the Canterbury earthquake, showing that SC can cause

94 contamination of gravel with silty fines and prevent drainage during shaking, thus resulting in loss

95 of performance.

96 After the 1991 Loma Prieta earthquake, mitigation strategies against liquefaction in silty sands were

97 also analyzed by Mitchell and Wentz (1991), who compared the performance of sites reinforced by

98 SC with that of adjacent untreated areas. Minor or negligible damage was observed in the improved

99 soils, whereas cracks and/or settlements, primarily due to liquefaction, occurred in untreated soil

100 deposits. However, as the non-plastic fines content increased, the SC technique appeared to be more

101 successful in combination with pre-installed wick drains (Adalier et al., 2003). Gianella and

102 Studelin (2017) studied the behavior of sands and silty sands treated by TDP in South Carolina,

103 proposing this technique as a suitable and potentially sustainable ground improvement alternative.

104 Significant increases in cone resistance were observed after installation, though followed by a

105 reduction in the long term. Finally, Li et al. (2018) reported a series of in-situ tests and full-scale

106 field tests to investigate the RCM compaction effects on laterally loaded piles in silts and silty sands

107   in eastern China, showing that this approach results in increase lateral resistance of the piles as well

108   as in a reduction in soil liquefaction potential.

109   The increase in penetration resistance due to the installation of the ground improvement techniques

110   described previously is generally attributed to the increase in soil density alone, erroneously

111   neglecting the influence of lateral stress. Nonetheless, it has been observed (Harada et al., 2010;

112   Salgado et al., 1997) that the potential increment of lateral pressure can go well above the normally-

113   consolidated state, thus contributing to the increase of the liquefaction resistance within the

114   improved soils. In addition, it is still uncertain how to accurately account for the composite action

115   of discrete elements and soil. Soil-cement columns or grids constructed by cement deep soil mixing,

116   jet grouting, or other methods (e.g. SC) are considered effective for mitigating liquefaction in silty

117   sands by shear reinforcement mechanism (e.g. Mitchell, 2008; Adalier and Elgamal, 2004).

118   However, recent numerical studies by Rayamajhi et al. (2014, 2016) and Green et al. (2008)

119   demonstrated that discrete columns may deform in both flexure and shear, being less effective in

120   reducing shear stresses than what shear stress compatibility implies. Investigations based on

121   vibroseis "T-Rex" and/or cross-hole tests in New Zealand and Ecuador (Wissmann et al., 2015;

122   Smith and Wissmann, 2018) provided evidence that RAP reinforced ground is significantly stiffer

123   than the untreated natural soil.

124   The level of shear stress reduction in the surrounding soil due to the in-situ installation of discrete

125   columns has still not been demonstrated by field data. Therefore, full-scale liquefaction tests in the

126   field, under controlled conditions, are important for a proper quantification of lateral stress and

127   shear stiffening phenomena. These tests will improve understanding of the behavior of the soil and

128   column composite response under conditions similar to those induced by earthquakes.

129   Previous experiences in the United States and New Zealand (e.g. Ashford et al., 2004; Wentz et al.,

130   2015; Saftner et al., 2015; Gianella and Stuedlein, 2017) show that liquefaction can be induced and

131   monitored in clean sands with controlled blasting. Some efforts have also recently focused on

132   studying the behavior of siltier deposits during blast-liquefaction tests in Italy (Amoroso et al.,

2017; Fontana et al., 2019; Passeri et al., 2018; Pesci et al., 2018). Furthermore, little research is available to demonstrate RAP effectiveness in mitigating liquefaction in sandy silts and silty sands, using blast-induced liquefaction. Nevertheless, preliminary results from a silty sandy case history in Ecuador suggest that RAP ground improvement elements installed beneath a 700 m-long bridge embankment prevented lateral spreading and settlement during the 2016, M_w 7.8 Muisne earthquake (Smith and Wissmann, 2018).

In this context, full-scale blast tests were performed at a silty sand site in Bondeno (Ferrara, Italy) where liquefaction was observed after the 2012 Emilia-Romagna earthquake (Emergeo Working Group, 2013), as preliminarily presented by Amoroso et al. (2019). Compared to previous blast experiences, the present study is based on a multidisciplinary approach, involving a team of forty researchers with expertise in the fields of geology, geophysics, geotechnical engineering and site surveying, in order to gain a comprehensive understanding of the mechanisms governing the selected engineering solution for liquefaction mitigation. Geotechnical testing, surface seismic and geoelectrical surveys were performed before and after RAP installation, as well as after blasting, to verify the effectiveness of the treatment. An array of explosive charges was detonated sequentially on improved and unimproved test areas to evaluate relative liquefaction resistance after RAP installation, monitoring excess pore pressures, settlements and accelerations. Also, four small exploratory trenches were dug to identify deformational features related to the blast tests and to characterize the fractures/conduits used by the liquefied sands during blast tests and in the 2012 earthquake. Samples of ejecta and in-situ sand were collected to characterize the soil deposits with geotechnical and/or petrographic laboratory tests. This combination of geological and geotechnical methods appears to be vital for a proper interpretation of the liquefaction process and for verifying the seismic origin of dykes (Obermeier, 1998). The paper describes the testing program and presents insights from this multidisciplinary study.
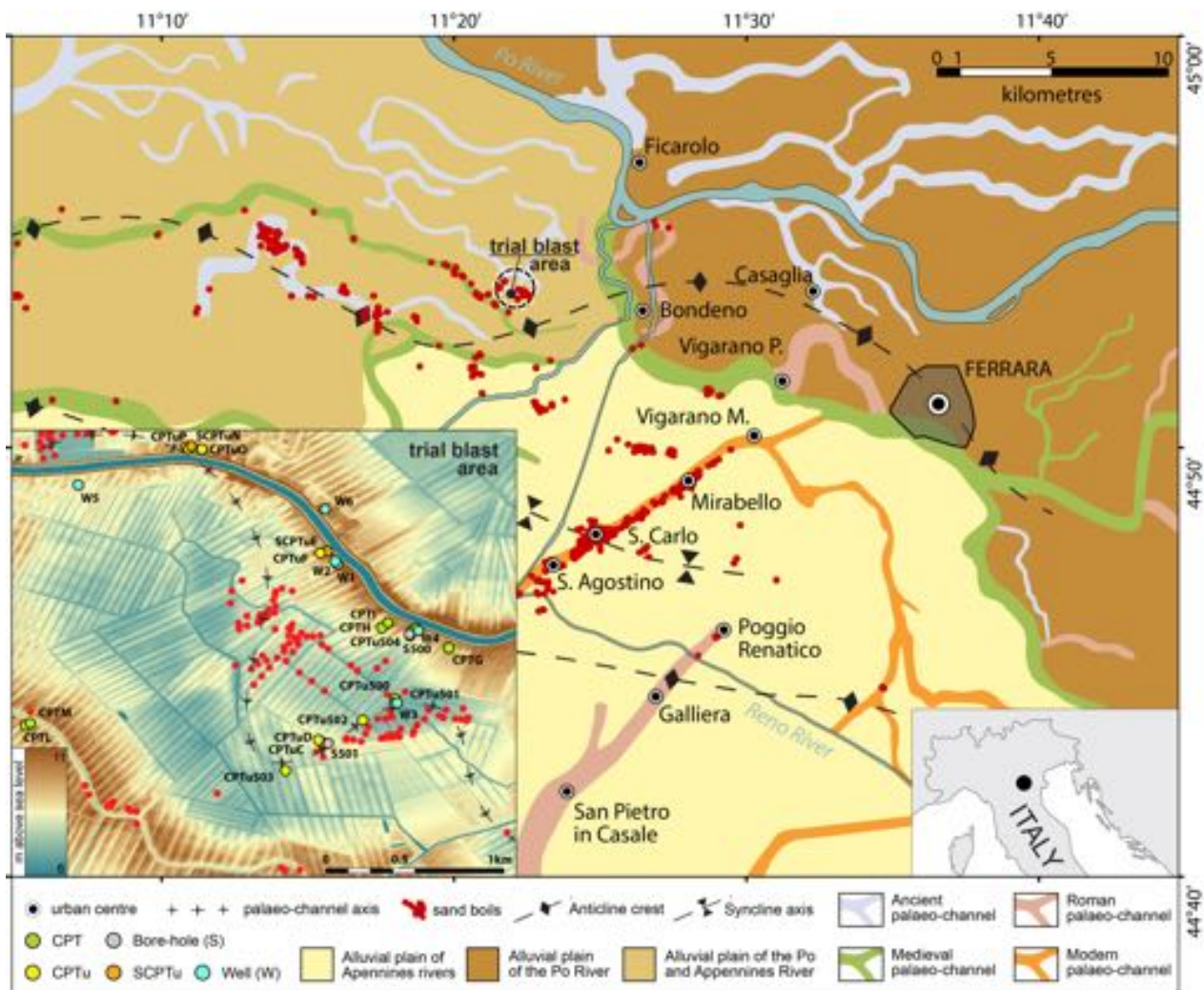
2. Geology, geomorphology, and seismotectonic framework of the study area

2.1. Geological setting

The blast test site area is located in the south-eastern portion of the Quaternary alluvial plain which extends between the southern Alps and the northern Apennines. This plain is one of the deepest alluvial plain in Europe, though the exact depth of the seismic bedrock and the relevant seismic-wave properties are still a matter of debate among researchers (Molinari et al., 2015). The test site lies on the buried external portions of the Apennine chain, consisting of seismically active fault-fold structures (Toscani et al., 2009). The sedimentary units involved in the experiment accumulated during the late Pleistocene and Holocene periods, and show significant lateral variability in thickness (Minarelli et al., 2016). The latest Pleistocene unit is part of a depositional cycle typically referred to as Villa Verrucchio Subsynthem (AES7), whereas the Holocene sediments pertain to the Ravenna Subsynthem (AES8). Several generations of fluvial channel deposits were fed from the south by the Apennine streams and from the west by the Po River (Fig. 1).

Fig. 1. Map of the paleochannel bodies (modified after Stefani et al., 2018), of the surface manifestations of liquefaction following the 2012 Emilia-Romagna earthquake (Emergeo Working Group, 2013) and of the location of the blast area. The traces of the main anticline crest and syncline axis of the buried tectonic belt are also depicted. The lower-left corner shows the geomorphological features from LIDAR map together with the available investigations and the 2012 sand boils.

2.2. Seismic activity and effects

The area has a seismic history of low- to moderate-magnitude events. The most relevant past event is the VIII MCS (moment magnitude M_w 5.5) 1570 earthquake that struck the area of Ferrara, causing liquefaction phenomena, open fractures and changes in channel water flows (Caputo et al.,

2016). In May 2012, a seismic sequence affected the area with two main shocks (Pondrelli et al., 2012). The first occurred on May 20th (M_w 6.1), with an epicenter at about 15 km to the south-west of the test site, followed by aftershocks up to M_w 5.1. The second main seismic event took place on May 29th (M_w 5.9), with an epicenter located at about 24 km to the south-west of the test site. The highest peak ground accelerations (PGA) recorded at nearby strong-motion stations located in the epicentral area turned out to be approximately 0.3g and 0.9g, for the horizontal and vertical components, respectively (Luzi et al., 2013). Both main shocks induced important secondary effects at the surface, such as widespread liquefaction, sand boils (Fig. 1) and ground failures, together with lateral spreading and differential settlements. Sand boils and liquefaction manifestations occurred mainly along paleochannel deposits (Fig. 1).

2.3. Geomorphological framework

A strong link between the geographic distribution of the fluvial sand deposits and the location of liquefaction events was observed for the 2012 seismic crisis (e.g. Papathanassiou et al., 2015; Caputo et al., 2016) using satellite images and high-resolution LIDAR topographic models (Civico et al., 2015). The detected geomorphological features were also documented by the comprehensive database of subsurface investigations collected for the ongoing seismic microzonation (Fig. 1) and by other studies (Amoroso et al., 2020; Tonni et al., 2015).

The selected test site, which experienced the occurrence of a large number of sand boils (Fig. 1) during the 2012 seismic sequence (Emergeo Working Group, 2013), is located above a meander point bar structure. This meander morphology is partially confined by younger higher fluvial ridges bordering the test area in the south and the north (Fig. 1) and forming an interfluvial depression.

2.4. Stratigraphic organization

The fluvial sediments at the test site belong to three superimposed units, related to different depositional environments and chronological intervals (Figs. 1 and 4):

209 (a) the lower unit consists of fluvial medium-grained sands and silty sands, deposited during the late

210 glacial maximum (Pleistocene) into a braided river channel system (upper portion of AES7 unit).

211 This unit is about 20 m-thick topped by a regional paleosoil surface, overlain floodplain fine-

212 grained sediments. At the test site, the top of this unit corresponds to the erosive base of a Holocene

213 fluvial channel sand body;

214 (b) the middle unit is formed by fluvial sandy silts, laterally grading into argillaceous sediments.

215 This unit is approximately 9 m-thick (AES8 unit, Holocene). The interpretation of satellite images

216 and topographic data, coupled with information obtained from subsurface logs, suggests that the

217 sand accumulated into a meandering channel of the Po River. At the test site, this unit is buried at a

218 shallow depth. The liquefaction induced by the blast test largely took place within this unit;

219 (c) the upper unit comprises fluvial clays and silts (3 m-thick) forming the uppermost part of the

220 AES8 unit, deposited during the final infilling of the fluvial channel, probably recording influxes

221 from Apennine-derived rivers.

222

223 **3. Description of the field activities**

224 The blast tests activities were conducted over a period of one year (November 2017-October 2018),

225 as listed in Table 1.

226 Table 1. Activities associated with blast tests at Bondeno site.

Phase	Activity	Period
I	Preliminary investigations for site selection	November 2017-January 2018
II	Geotechnical and geophysical tests for characterization of the test site	February-March 2018
III	RAP column installation	March-April 2018
IV	Geotechnical and geophysical tests one month after RAP installation	April-May 2018
V	Installation of blast holes, profilometers, accelerometers, pore pressure transducers	May 2018
VI	Blast tests	4 June 2018
VII	Geotechnical and geophysical tests soon after blast tests	June 2018
VIII	Geotechnical and geophysical tests one month and a half to two months after blast tests	July-August 2018
IX	Geological, geotechnical and geophysical tests three to four months after blast tests	September-October 2018

227

228 From November 2017 to January 2018, preliminary investigations were aimed at identifying the

229 most suitable test site. This choice was guided by the need to select a shallow liquefiable layer of

230 silty sands, also taking into account the previously mentioned geomorphological considerations and

231 2012 liquefaction evidences. Furthermore, the site was located at a distance from buildings and

232 human activities of this area in order to minimize the effect of vibrations generated by the

233 detonation.

234

235 **3.1. Pre-blast activities**

236   **3.1.1. Pre-RAP investigations**

237 From February to March 2018 an intensive geotechnical and geophysical campaign was carried out

238 in order to achieve a detailed characterization of the upper 20 m of the subsoil, also useful for the

239 design of the RAP columns and the blast tests. These surveys allowed identifying a relatively

240 homogeneous area (60 m x 40 m), where two blast panels - one for testing the natural soil (Natural

241 Panel, NP) and one for the improved soil (Improved Panel, IP) - were eventually placed (Figs. 2a

242 and 2b). Later investigations were all concentrated in these two relatively small circular areas

243 spaced 20 m apart, each having a diameter of 10 m. The geotechnical investigations, pushed to

244 approximately 15 to 20 m in depth, consisted of: (i) two boreholes, one in the IP and one in the NP,

245 along with standard penetration testing (SPT) and disturbed soil sampling for grain size distribution

246 analyses, determination of Atterberg limits, petrographic analyses and radiocarbon dating; (ii) two

247 piezocone (CPTU) tests, one in the IP and one in the NP; (iii) one seismic dilatometer (SDMT) test

248 in the IP. The geophysical surveys consisted of: (i) five electrical resistivity tomography (ERT)

249 alignments, spaced at 2 to 5 m and 63 m long (64 electrodes for each line), crossing the IP and the

250 NP; (ii) one active P-wave and S-wave tomography, 71 m long, performed using firstly 72 vertical

251 geophones and secondly 72 horizontal geophones along the same line; and (iii) one passive 2D-

252 rectangular array (24 m x 21 m) using 72 P-wave geophones spaced at 3 m, and centered in the IP.
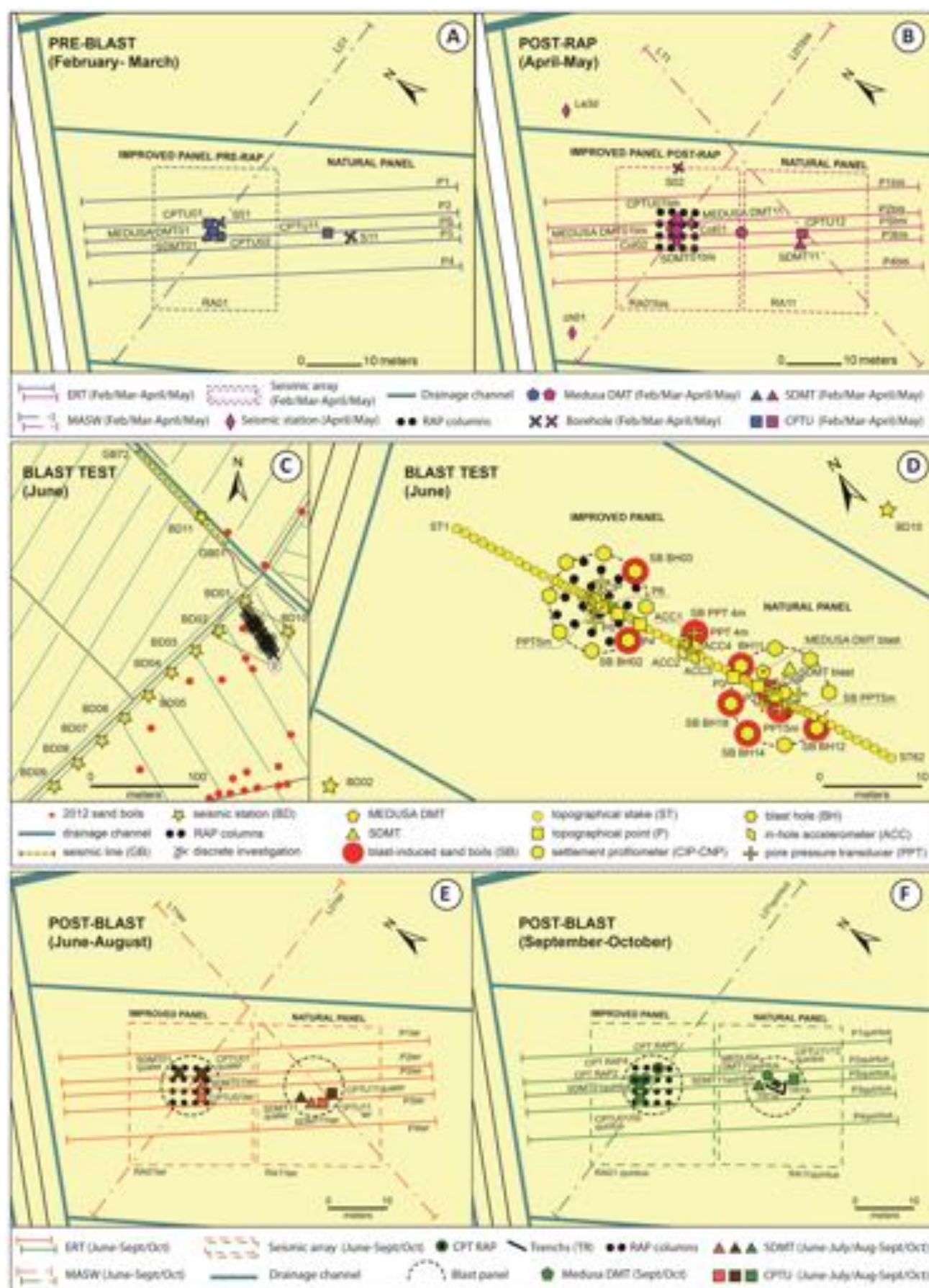
Fig. 2. Map of the investigations at the test site carried out pre-blast in February-March 2018 (a), post-RAP in April-May 2018 (b), during blast at small (c) and large (d) scale, post-blast in June-July-August 2018 (e) and in September-October 2018 (f).

Grain size analyses were carried out using a Mastersizer 3000 particle size. Compositional analyses under transmitted light microscopy were performed on the 0.125–0.250 mm fraction, according to the Gazzi-Dickinson method, designed to minimize the dependence of the analysis on the grain-size (Fontana et al., 2015).

Prior to RAP installation, a 0.5 m-thick, geosynthetic-reinforced, gravel platform was set up to allow the access of the RAP installation equipment machinery. Moreover, an additional CPTU was performed to check the IP homogeneity, and a SDMT was also performed within the NP.

3.1.2. RAP installation

Between the end of March and the beginning of April 2018, a 4x4 quadrangular grid (2 m center-to-center spacing) of RAP columns, each 9.5 m long, was built (Fig. 2). The final diameter of each pier was 0.5 m with an associated area replacement ratio, defined as the ratio of the pier area to the tributary soil area surrounding the pier, equal to 5%. Because of construction issues, the last column of the third line was limited to only 5.5 m depth. For quality control of the ground improvement work, ten RAPs were subjected to aggregate flow rate tests and crowd stabilization tests in order to evaluate the pier gravel volume and to measure the column stiffness, respectively. These tests revealed a reduced effectiveness of the construction procedure for the upper-left piers.

The RAP elements were constructed using a displacement technique with an excavator mounted mobile ram base machine fitted with a high frequency (30 to 40 Hz) vertically oscillating hammer as illustrated in Fig. 3.
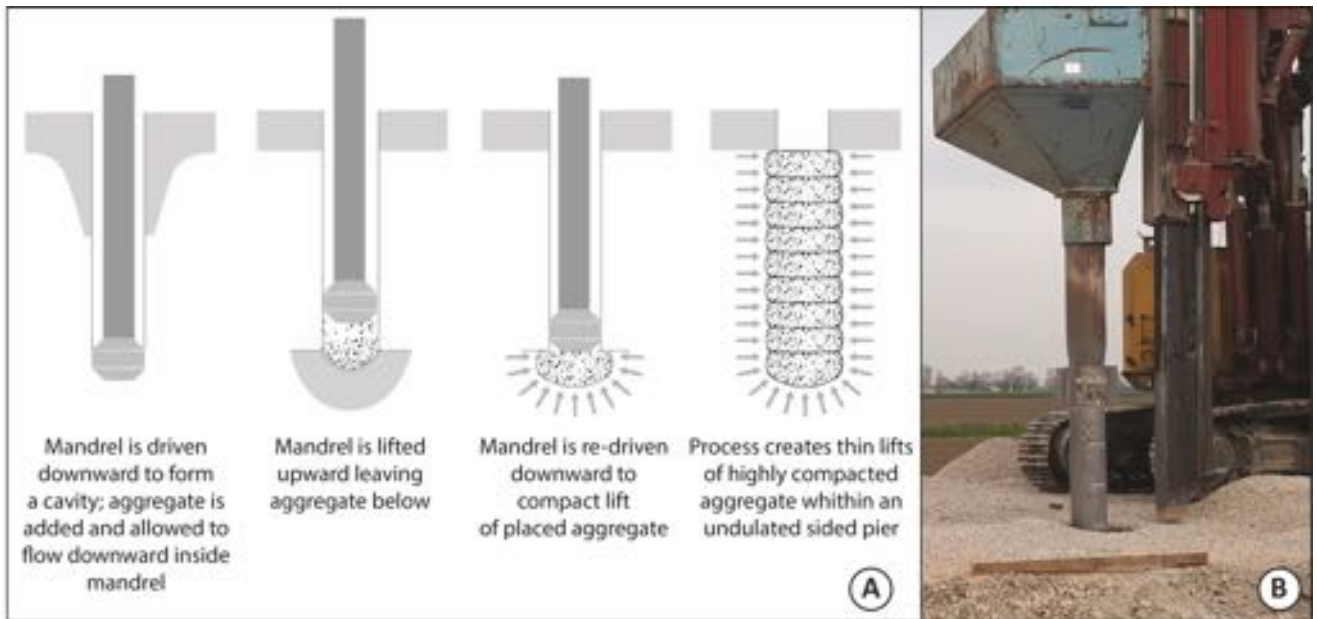
Fig. 3. (a) RAP column installation scheme with vibratory hammer and hopper/mandrel for gravel installation (Wissmann et al., 2015); (b) RAP installation at Bondeno test site.

The base machine drives a 300 mm outside diameter open-ended pipe mandrel fitted with a unique specially-designed 360 mm diameter tamper foot into the ground. Proprietary internal restrictor elements prevent soil from entering the mandrel during driving and serve as an internal compaction surface during tamping. After driving to the designed depth, the hollow mandrel serves as a conduit for aggregate placement. Placed inside, the aggregate flows to the bottom of the mandrel. The tamper foot and mandrel are then raised approximately 0.9 m and then driven back down 0.6 m, forming a 0.3 m-thick compacted lift. Compaction is achieved through static down force and dynamic vertical ramming from the hammer combined with the confinement of the tamper's restrictor elements. The process densifies aggregate vertically and the beveled tamper foot forces aggregate laterally into cavity sidewalls. Crushed gravel (typically graded at 10 to 40 mm in particle size) is fed through the mandrel from a top mounted hopper and compacted in the displaced cavities to create approximately a 0.5 m-diameter, dense, stiff, aggregate pier element. The construction methodology has been described in detail by Saftner et al. (2018).

3.1.3. Post-RAP investigations

At the end of April 2018 supplementary geotechnical tests were carried out in the middle of four piers (Fig. 2b) and pushed to a maximum depth of 15 m, in order to evaluate the RAP effect on soil response one month after construction. DMT soundings were performed using a new device, the Medusa DMT, that is a combination of the flat dilatometer with hydraulic automation and a measuring system for autonomously performing DMT tests (Marchetti et al., 2019).

At the beginning of May 2018, the temporary gravel platform was removed to allow additional geophysical surveys with the same configuration as the original investigation (Fig. 2b): (i) five ERT alignments; (ii) two active P-wave and S-wave tomographies, one in the IP and one in the NP; (iii) two passive 2D-rectangular arrays, one centered in the IP and one centered in the NP; and (iv) four surface seismic stations, equipped with three-components Lennartz-5s velocimeter, two in the treated area and two in the natural soil.

3.2. Blast activities

In May 2018, blast holes, profilometers, accelerometers, pore pressure transducers, seismic DMT and Medusa DMT equipment were installed in the ground. Topographical reference points, seismic stations and geophones were placed on the surface in preparation for the blast tests that took place on June 4th, 2018 (Figs. 2c and 2d). Locations of the instrumentation relative to the blast holes for each panel are shown in Fig. 2d.

Eight blast holes (BH), 7 m deep and equally distributed along a 5 m-radius ring, were drilled in each panel. Charges were located in each BH at 3.5 m (0.5 kg) and 6.5 m (2.0 kg) within the potentially liquefiable layer. This soil layer was detected between 3 and 8 m depth according to a preliminary assessment of liquefaction susceptibility, that considered a design earthquake for a 475 years return period ($M_w = 6.14$ and $PGA = 0.22g$, Amoroso et al., 2019).

At the center of each panel, a profilometer (CNP for the natural panel and CIP for the improved panel) was anchored at 15 m depth to record the settlement vs. depth profile. In fact, previous

322 experiences worldwide (e.g. Amoroso et al., 2017; Gianella and Stuedlein, 2017; Finno et al., 2016)

323 provided evidence of a bowl shaped displacement surface following blasting. Furthermore, from the

324 previous blast experiment carried out in a site of the Po River valley, it was observed that

325 settlements in the circular blasting area were similar to liquefaction-induced vertical displacements

326 predicted for a M_w 7.5 earthquake in the same depth interval (Amoroso et al., 2017).

327 To estimate blast-induced shear strains and shear stresses, four in-hole 200g triaxial

328 microelectromechanical (MEMS) accelerometers (ACC) were located at approximately midway

329 between the two panels (i.e. about 10 m from CNP and CIP), using a 1 m-squared configuration

330 between 3.5 and 4.5 m deep and recorded at a sampling rate of 1000 Hz. Pore pressure transducers

331 (PPT) were installed from 4 to 9 m at each meter of depth, within the liquefiable layer (1 or 2 m

332 distance from the center of each panel) to measure the generation and subsequent dissipation of the

333 excess pore pressures induced by the blasts in the silty sand deposits of both panels, at a sampling

334 rate of 100 Hz. An additional PPT was set up at an average depth of 4 m in the middle of the

335 accelerometer array to study the non-linear soil response induced by the blast-liquefaction, coupling

336 the shear strains with the excess pore pressures. A SDMT and a Medusa DMT were finally installed

337 at 6.1 m deep in the natural panel to monitor the variation of shear wave velocity with excess pore

338 pressure following the blasts.

339 Six survey rods (P) were located within the NP and the IP and an alignment of sixty-two survey

340 stakes (ST) crossing both panels was set up to record the vertical ground surface settlements over

341 time after the blasts and to integrate with the profilometer data, Terrestrial Laser Scanning (TLS),

342 and Structure from Motion (SfM) aerial photogrammetry. A line of seventy-two P-wave geophones

343 (GB, 4.5 Hz) was installed at an average distance of 100 m from the blast area, while eleven surface

344 seismic stations (BD), each of them composed of a velocimeter (Lennartz-5s) and an accelerometer

345 (Episensor-1s), were located along a Y-shaped configuration, having the closest and the farthest

346 stations at 25 and 250 m, respectively (Fig. 2c), to record the particle motion with distance and to

347 verify the level of vibration generated by the detonation.

Explosives were detonated on June 4th, with a microdelay of 1 second between subsequent charges and starting the detonation from the bottom (6.5 m deep) to the upper level (3.5 m deep). The blasts of the two panels were designed separately (i.e. blast #1 for the NP and blast #2 for the IP) to limit effects of superposition and consequently to study the effect of the blast-induced liquefaction on the IP and the NP separately.

Surface movements induced by underground explosions and liquefaction effects were observed by means of TLS and SfM surveys performed before and after each blast test providing and comparing multi-temporal Digital Terrain Models (DTMs). Unmanned Aerial Systems (UAS) equipped with DJI FC6310 and DJI FC350 cameras and a Teledyne Polaris scanner were used. The results from TLS dense point clouds, characterized by a mean 5 mm sampling step, provide a complete description of subsidence rates in the area following liquefaction and pore pressure dissipation.

3.3. Post-blast activities

Three post-blast investigations were performed in June, July-August and September-October 2018 (Figs. 2e and 2f), with the aim of comparing the variation with time of the geotechnical and geophysical parameters before and after the blast tests in both panels.

Two piezocone and two seismic dilatometer tests were carried out up to 15 m deep, in the IP and the NP soon after the blast tests. Moreover, in June 2018 ERT surveys and active and passive geophysical surveys were performed using the same configuration of the previous investigations shown in Fig. 2e.

One month and a half to two months after the blast tests, an additional in-situ testing campaign was repeated: two CPTUs and two SDMTs were performed, up to 15 m deep, between piers and within the untreated area, as shown in Fig. 2e.

Finally, three to four months after blasting, the last geotechnical and geophysical tests were carried out, as reported in Fig. 2f. As for the previous investigations, CPTUs, SDMTs and Medusa DMTs were performed in the IP and the NP, pushing tests to a maximum depth of 15 m. Moreover, three

mechanical cone penetration tests were performed at the center of RAP piers (CPT RAP) to a depth of approximately 11 m. In September-October 2018 ERT, active and passive geophysical surveys were repeated again using the same configuration of the previous investigations.

At the conclusion of the experimental activities, four small exploratory trenches were dug across the liquefaction-induced sand boils within the natural panel (Fig. 2f). The excavations were performed to better understand the blast-induced liquefaction mechanism but also to identify and characterize the fractures/conduits used by the liquefied sands in the 2012 earthquake (Amoroso et al., 2017) and possibly during older events (De Martini et al., 2012; Caputo et al., 2016). Moreover, sand samples were collected from the fractures as well as from the surface (sand boils) in order to study the variability in grain size potentially related to the liquefaction process and to the liquefied sand paths (Fontana et al., 2019).

4. Main geotechnical features from the pre-blast investigations

The interpretation of all the geotechnical and geophysical investigations performed in both panels (IP, NP) prior to improvement was used to define a representative stratigraphic model of the natural subsoil (Fig. 4a). The identified soil units are listed below and classified in terms of the Unified Soil Classification System (USCS), according to ASTM D2487-11 (2011):

(i) top soil (CH) from the ground surface to 0.8 m;

(ii) clays and silts (CL) from 0.8 to 3.4 m;

(iii) silty sands (SM) from 3.4 to 12.6 m (paleochannel of the Po River);

(iv) sandy silts (ML) from 12.6 to 13.4 m (well-drained interfluvial deposits);

(v) sands and silty sands (SM-SP) from 13.4 to 15.6 m (glacial braided Po River deposits).

The silty sands (SM) and sandy silts (ML) have laterally a variable thickness due to their channel-filling nature. In this respect, the ML layer can vary in depth between 11.70 and 13.40 m, and have a minimum thickness of approximately 0.5 m.
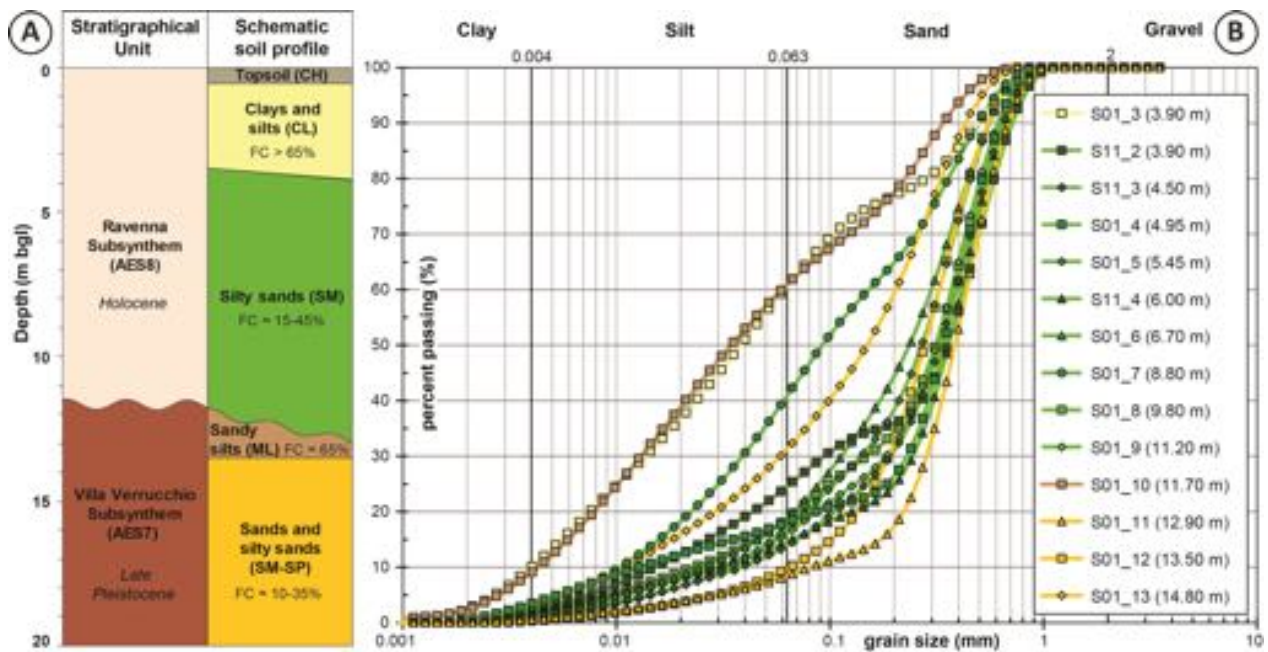
Fig. 4. Average subsoil profile at the test site and stratigraphic units (a) and grain size analyses (b).

Fig. 4b shows the results of the grain size analyses performed on the disturbed samples from S01 and S11 boreholes. The analyzed samples range from silty sands to silts with a variable amount of sand and clay. The majority of samples fits in a relatively narrow range, predominantly made up of fine sands; the content of silt is on average less than 25% and clay is < 5%. A higher percentage of fine sediments can be found in the shallowest sands (3.9 m depth) or in thin lenses detected at 8.8, 11.7 and 14.8 m depth. In particular, Fig. 4 shows that the SM layer has a fine content $FC \approx 15$-45%, while $FC \approx 65\%$ for the ML layer and $FC \approx 10$-35% for the SM-SP layer.

Sands from cores S01 and S11 have a quartz-feldspar rich composition and are made up of quartz, feldspars and subordinate lithic fragments. Siliciclastic lithics include low-grade metamorphic rocks, shales and spillite and carbonate lithic. Crystals of muscovite, chlorite and biotite are also present as well as heavy minerals. The composition of the sands show a clear affinity with sands from the Po River.

With reference to the defined stratigraphic model, Fig. 5 shows the soil response prior to RAP installation in terms of corrected cone resistance (q_t) from CPTU test, horizontal stress index (K_D) and shear wave velocity (V_S) from the SDMT test. The variation of q_t and K_D profiles with depth

looks related to the geologic depositional environment. Below the fine-grained units detected in the upper 3.4 m, the paleochannel of the Po River (from 3.4 to 12 m) is characterized by different q_t and K_D values when compared with glacial braided Po River deposits (below 13.4 m). In contrast, the V_S increases consistently with the effective vertical stress.

Fig. 5 also provides interpretations of CPTU measurements in terms of the soil behavior type index (I_{cn}), fines content (FC) according to Robertson and Wride (1998), and relative density (D_R) computed with the correlation proposed by Jamiolkowski et al. (2003). The computed FC values appear to be generally underestimated in comparison with those obtained from laboratory tests (blue dots in Fig. 5). However, at the test site the dataset is currently too small to develop a site-specific correlation that would take into account the uncertainties related to FC-I_{cn} relationship (e.g. plasticity and mineralogy).
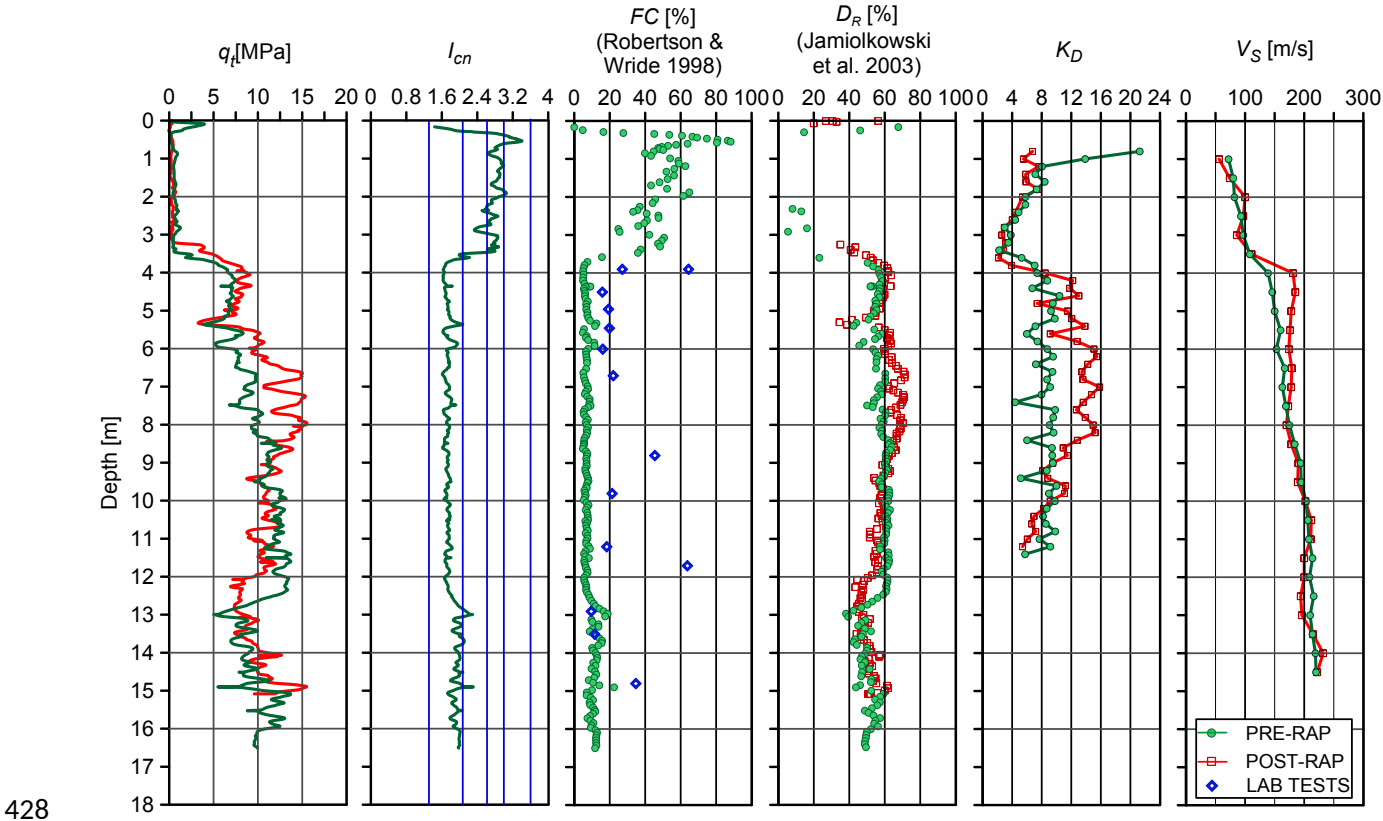
Fig. 5. CPTU and SDMT profiles pre/post RAP installation.

## 5. Main outcomes from the experimental activities

5.1. Post-RAP investigations

The site investigation performed one month after RAP column installation was helpful to understand the effectiveness of the ground improvement technique. Fig. 5 provides a comparison between field soil responses before and after treatment, in terms of both CPTU and SDMT profiles. A decrease of soil properties in the upper crust, partly due to the construction of the platform, but also to the low confinement induced by RAP installation and the seasonal variations in water content caused by fluctuation of the GWT from 1.5 m (February 2018) to 0.8 m (April 2018), is observed. Conversely, the layer between 3.4 and 9.5 m shows an increase in resistance and stiffness due to the installation of the piers. Unlike clean sands studied in New Zealand (e.g. Wissmann et al., 2015, Vautherin et al., 2017), in this case no improvement was detected in the silty sands below the toe of piers (Fig. 5). Looking in detail at the in-situ test data between 3.5 and 5.5 m depths, q_t and K_D increase on average from 7 to 8 MPa, and from 7-9 to 12, respectively. This trend is further confirmed in the underlying layer, between 5.5 and 9.5 m, where the natural soil is characterized by $q_t \approx$ 8-10 MPa and $K_D \approx$ 7-9, and the treated soil assumes values of $q_t \approx$ 10-14 kPa and $K_D \approx$ 13-15. Moreover, from 3.5 to 5.5 m in depth, the CPTU-based estimates of D_R shows a minor increase after pier installation, whereas a more significant increase is observed at 5.5-9.5 m (i.e. from approximately 60 to 70%). In contrast, V_S measurements show a limited improvement between 4 and 7 m depth, from 140-165 to 175-185 m/s, and remain constant below 7 m (Fig. 5). This tendency may be related to the decrease in vertical effective stress with some disturbance to the soil structure (e.g. Mitchell and Solimar, 1984), for RAP installation.

5.2. Blast test effects

Figs. 6a and 6b show the results of the aerial SfM survey after both blasts. It can be easily observed that liquefaction was induced in the NP, as clearly indicated by the widespread sand boil evidence in this location (see also Fig. 2d). In contrast, only minor liquefaction traces are observed within the

457 IP, mainly near the edge of the blast ring. These limited sand boils are, however, outside the limits

458 of the RAP group and likely developed in unimproved soils in this area.

459
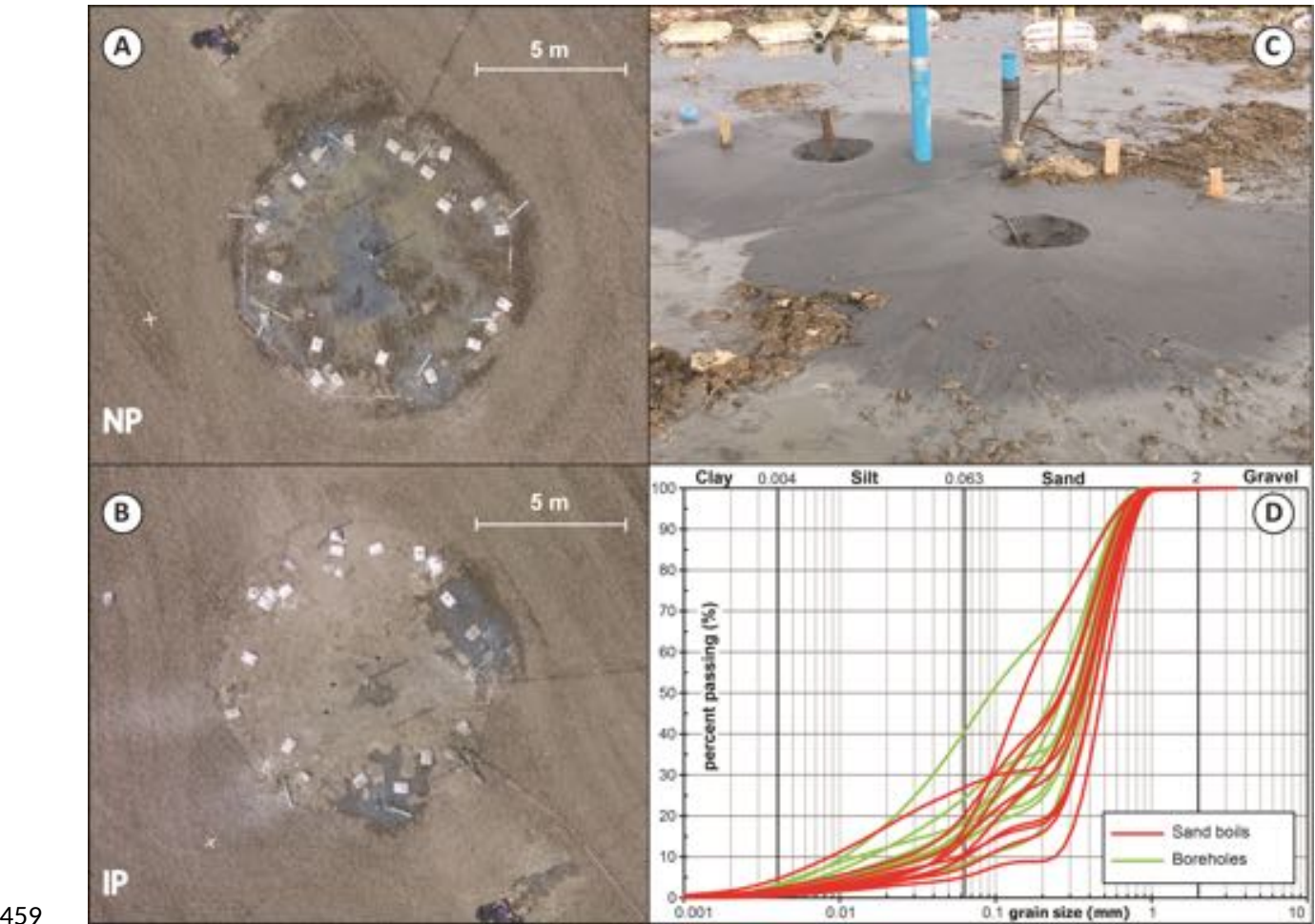
460 Fig. 6. SfM point cloud of surveyed area showing liquefaction-induced sand boils after blast #1 in

461 the NP (a) and blast #2 in the IP (b). Detail of the sand boils in the NP (c); grain size distributions of

462 the sand boils (in red) compared with sands from the boreholes (in green) (d).

463

464 Fig. 6c documents the sand boils induced by the blast in the NP after blast #1. Grain size

465 distribution analyses on soil samples collected from the sand boils (green curves in Fig. 6d) detected

466 medium-grained sands with a fines content varying between 6 and 28%. Compared to grain size

467 characteristics of the source beds (i.e. SM layer, red curves in Fig. 6d), a selective loss of fines can

468 be appreciated in the ejected sediments forming the sand boils, thus indicating that the liquefaction

469 process appears to preferentially select the grain diameters, as previously found by Fontana et al.

470 (2019), Maurer et al. (2019) and Cubrinovski et al. (2018).

471 Pore pressures measured by the PPT were used to compute excess pore pressure ratios ($R_u =$

472 $\Delta u/\sigma'_{v0}$) in the NP and the IP, where Δu is the measured excess pore pressure and σ'_{v0} is the initial

473 vertical effective stress prior to the blasts. Soil unit weights were interpreted from the SDMT tests.

474 In the NP, R_u values reached 1.0, indicating liquefaction, from a depth of 4 to 9 m. Plots of R_u

475 versus time after blasts are presented in Fig. 7 for transducers at a depth of 5 m in the IP and the NP.

476 In the NP, the blast sequence produced R_u values near 1.0 which persisted for 15 to 30 seconds (see

477 the zoom in Fig. 7) and then dissipated to near static levels in about 4 minutes. In the IP, peak R_u

478 values were somewhat lower ($R_u = 0.75$) than in the NP, but dissipated at a similar rate.

479 Settlement profilometers indicated that liquefaction, and subsequent reconsolidation, occurred

480 within a zone from about 3 to 11 m below the ground surface which is generally consistent with the

481 expected zone of liquefiable sediments. In the NP, volumetric strains were consistent with what

482 would be predicted by Zhang et al. (2002) if a M_w 7.5 earthquake had produced liquefaction from 3

483 to 11 m with a factor of safety of about 0.9. Volumetric strains in the same depth interval for the IP

484 were about 20% of those measured for the NP, despite excess pore water pressure values that

485 resulted in R_u values of 0.7 to 0.9.

486
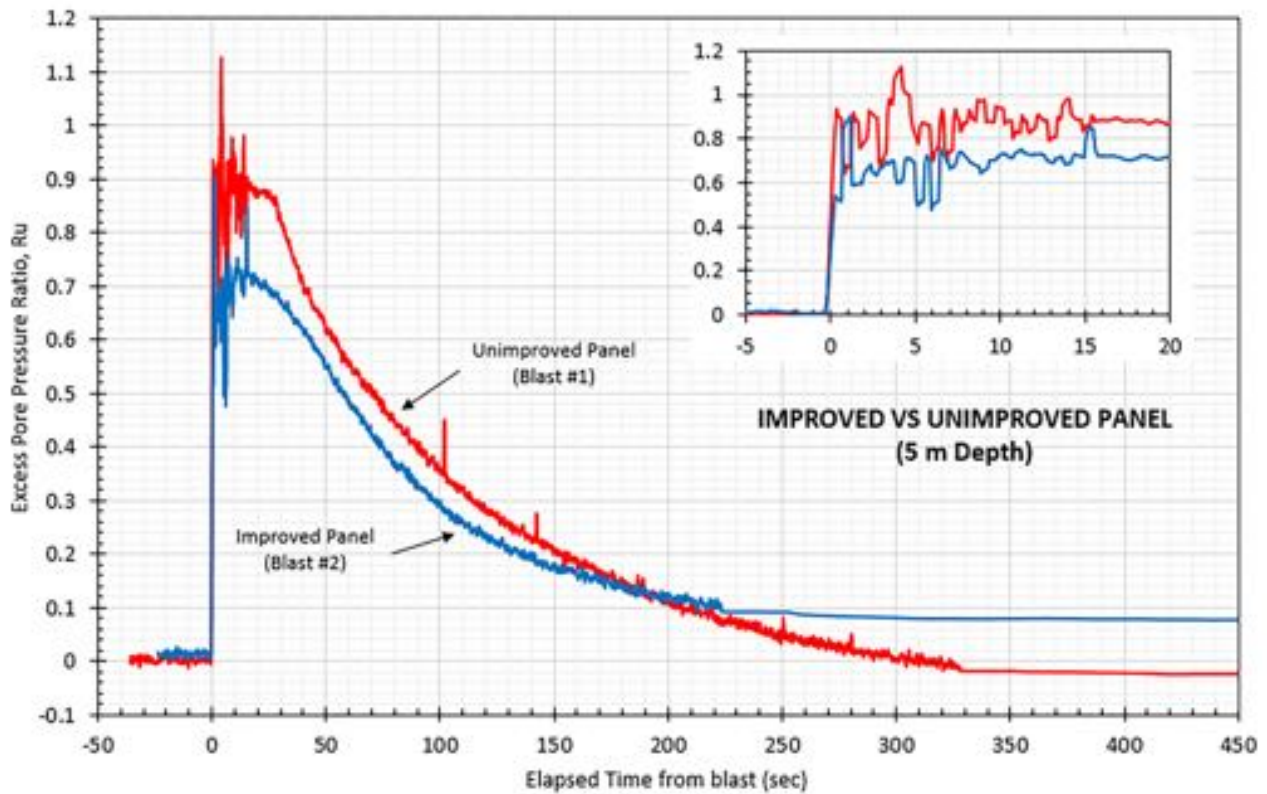
Fig. 7. Comparison of measured excess pore pressure vs. time curves for the IP and the NP at a depth of 5 m below the ground surface. For both panels the PPTs recorded at a sampling rate of 100 Hz and the R_u values were smoothed using a 100 point running average. This was done so that the residual excess pore pressure would not be obscured by the transient pressure spikes.

Fig. 8 shows color settlement contour maps obtained by comparing the TLS-based multi-temporal models with the terrain morphology maps. In the NP, after blast #1 there is clear subsidence of the area within the explosive charges, with a widely distributed settlement of about 6-8 cm. In contrast, after blast #2 only a few small sectors of the IP experienced settlement with an average of 2 cm (locally maximum 4-5 cm). For both blast tests, settlements were mainly delimited within about 10 m from the centers of the blast areas.

All topographical surveys indicate that settlements within the NP were on average between 7 and 10 cm, after both blasts. In contrast, settlements within the IP were between 2 and 5 cm. Liquefaction induced settlements in the NP would likely be excessive for many structures, whereas the reduced

501 settlements in the IP would likely be tolerable. The mechanisms responsible for the reduced

502 settlement in the panel treated with RAP columns may be related to soil densification and increased

503 lateral stress, but soil-pier interactions may also play a role. Due to the whole test setup the bearing

504 capacity was not evaluated, even though it is another important issue within liquefaction evaluation

505 criteria.
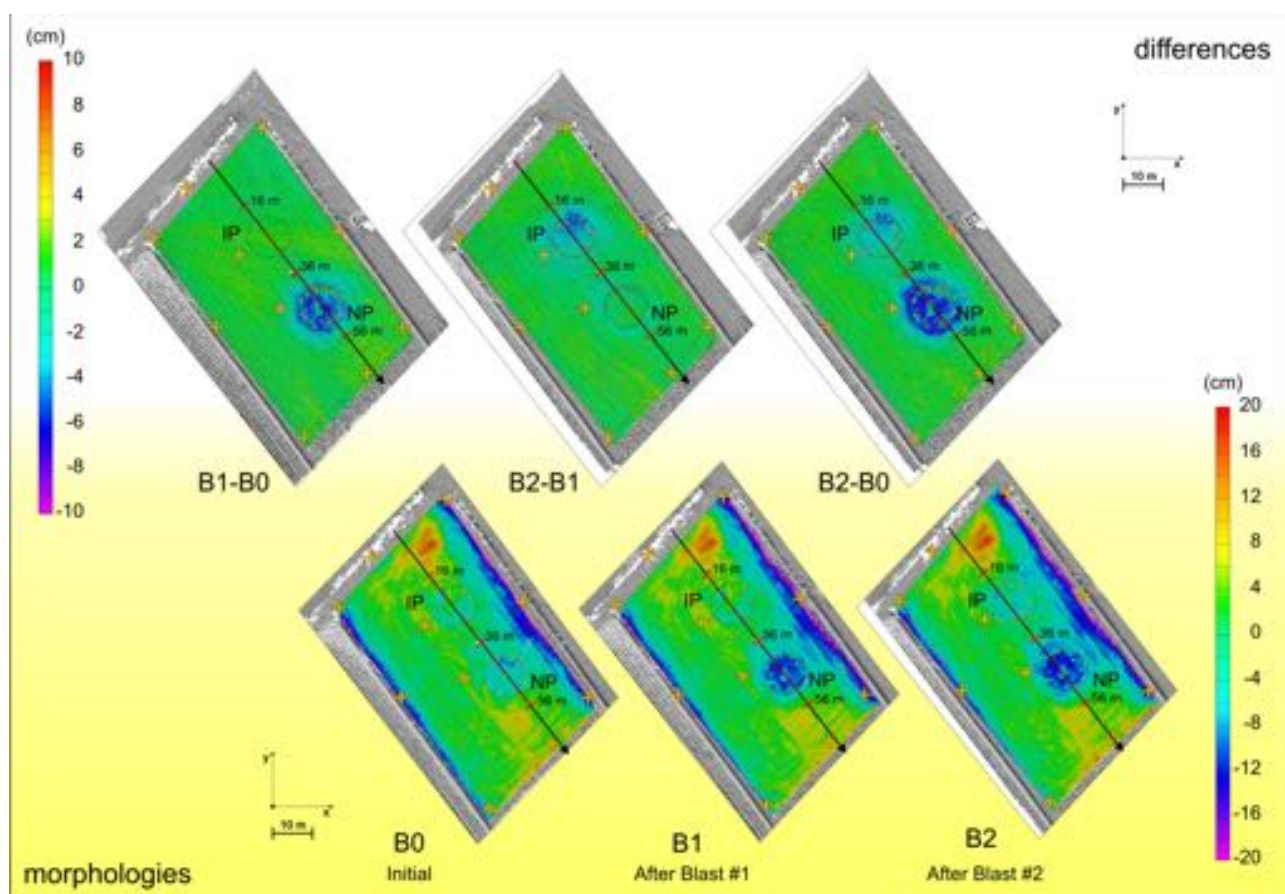
507 Fig. 8. Difference maps between TLS-based point clouds (upper panels), where BN-BM means N-

508 th point cloud compared with respect to the M-th one, and morphological maps (lower panels).

509

510 Fig. 9 shows the SDMT results recorded in the NP during both blasts. Soon after the blast #1, the

511 SDMT data show a shear wave velocity decrease to about 30% of its pre-blast value ($V_S \approx 49$ m/s

512 versus $V_S \approx 152$ m/s), while it took a few minutes to recover to approximately its initial value. For

513 blast #2, since the SDMT modulus was still installed in the NP, a smaller decrease of shear wave

514 velocity is observed, equal to approximately 5% of its pre-blast value ($V_S \approx 141$ m/s in place of $V_S \approx$

515　149 m/s), associated with a much faster recovery to its initial value. These results are consistent

516　with other previous experiences (e.g. Rollins et al., 2004; Mahvelati et al., 2016). Blast-induced

517　liquefaction reduces indeed the vertical effective stress and alters the soil fabric, thus causing initial

518　losses in soil stiffness (Mitchell and Solymar, 1984). However, the dissipation of the excess pore

519　pressure allows the soil to reconsolidate into a denser and more stable configuration (Narin van

520　Court and Mitchell, 1994) characterized by a higher soil stiffness, as confirmed also at the Bondeno

521　trial site by R_u and V_S data (Figs. 7 and 9).

522
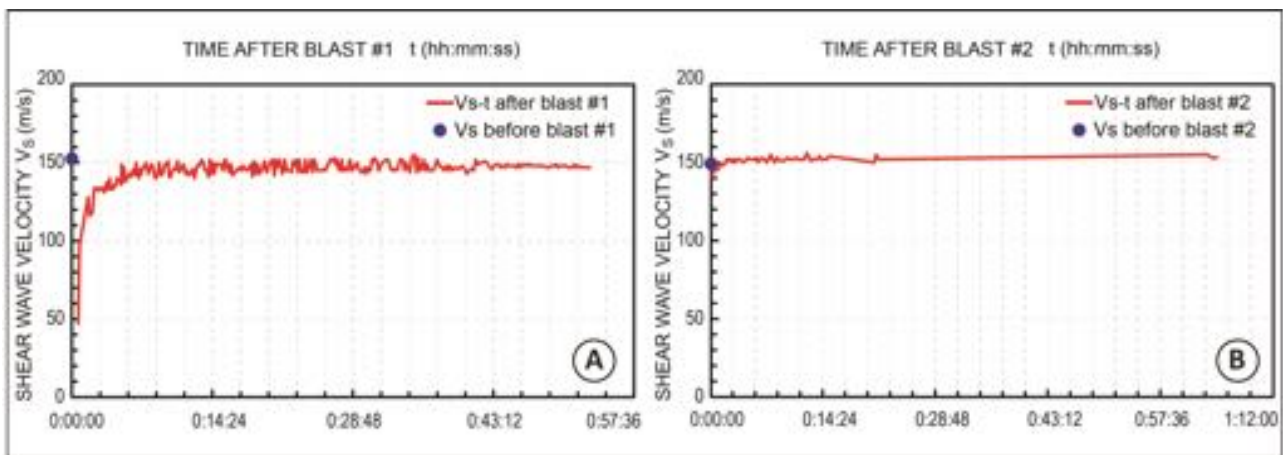
523　Fig. 9. Shear wave velocity data from seismic dilatometer during blasting: (a) blast #1; (b) blast #2.

524

525　All the seismic instruments installed prior to the blast tests (Figs. 2c and 2d) recorded the signals

526　produced by both detonations. Particularly, Fig. 10 shows some examples of time-series recorded

527　by the in-hole accelerometers. The detonations performed at 6.5 m depth produced very energetic

528　signals that are clearly recognizable in both the time and frequency domains (Fig. 10b). Instead, the

529　signals recorded at 3.5 m depth have generally lower amplitude, compared to the deeper ones, and,

530　in some cases, they are difficult to detect in the recorded time-series. The seismic data produced

531　during each blast are characterized by a very impulsive signal of short duration (about 0.02 s) and

532　high amplitude followed by a coda having a lower amplitude and a frequency content below 25 Hz

533　(Fig. 10b). For each detonation, the duration of the entire recorded signal does not exceed 0.4 s

534　(Figs. 10b and 10d). The maximum peak acceleration recorded by the in-hole sensors was of about

535 45g (ACC2-Y in Fig. 10c) and 52g during blast #1 (NP) and blast #2 (IP), respectively. In both

536 cases, the maximum acceleration was recorded by the Y-component of ACC2 sensor (Figs. 10a and

537 10d). From the spectrogram (Fig. 10b), the spectral content of the signals associated to explosions

538 reach the maximum resolvable frequency (Nyquist frequency at 500 Hz) with the adopted sampling

539 rate. Nevertheless, for each shot the maximum of signal was observed during the first impulse (Fig.

540 10c) with a duration of about 0.003 s, corresponding to frequency of about 300 Hz, a value lower

541 than the Nyquist frequency.
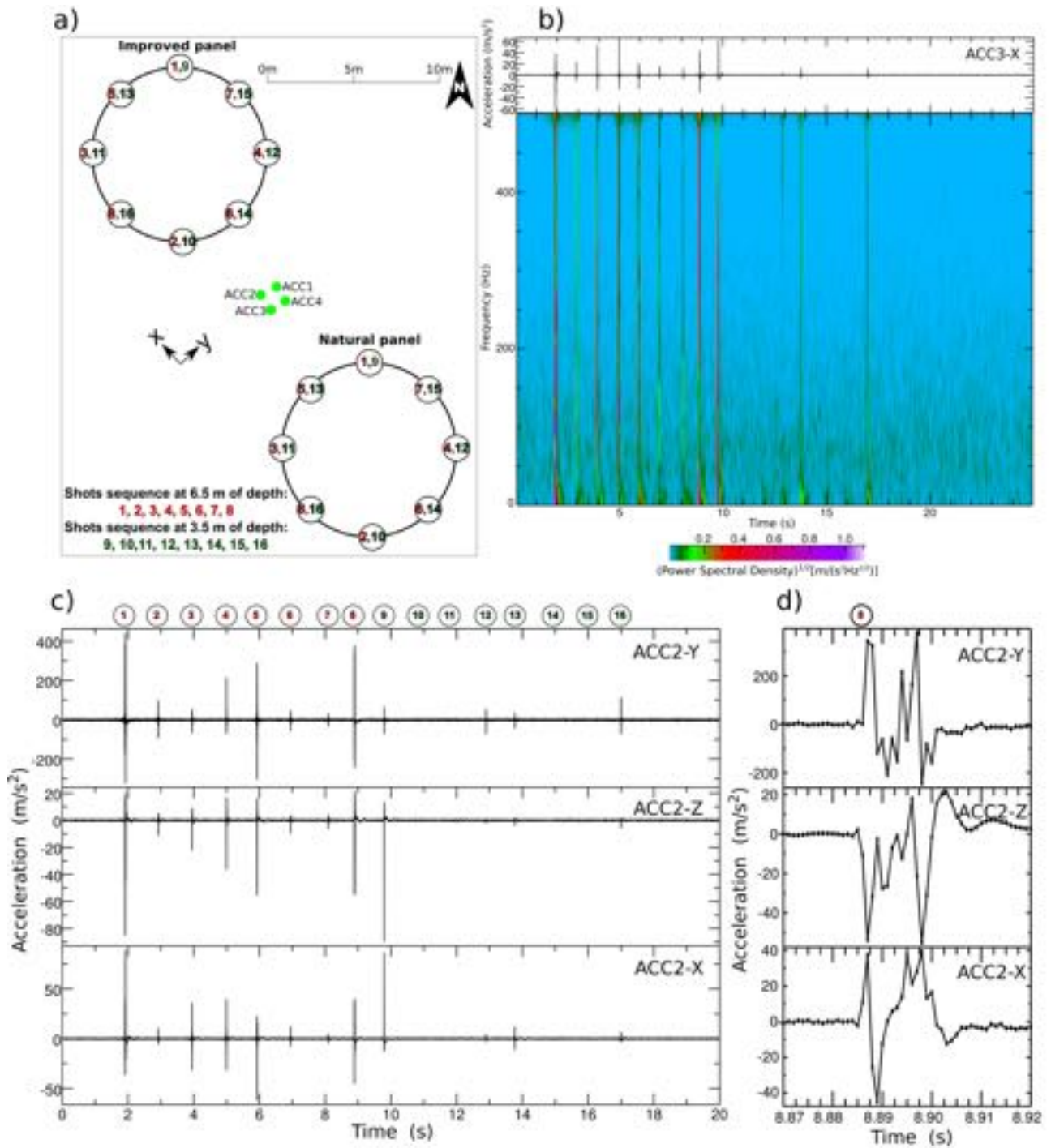
542

543   Fig. 10. Schematic diagram illustrating the locations (and the sequences) of charges detonated in the

544   NP and the IP with respect to the positions of the four installed accelerometers (ACC1, ACC2,

545   ACC3, ACC4) (a); seismic traces and related spectrogram recorded during blast #1 by the X-

546   component of ACC3 in-hole accelerometer (b); time histories of accelerations recorded during blast

547   #1 by the three different components of ACC2 accelerometer (c); zoom of signals recorded during

548   blast #1 by the different components of ACC2 during the shot number 8. The circles on the top of

549   Figs. 10c and 10d show the number of explosions associated with the recorded signals (d).

550

551   The seismic stations and the geophones permitted an estimate of the peak ground acceleration

552   (PGA) and peak ground velocity (PGV) values generated by both the blasts at distances between 20

553   and 250 m from the centers of the two panels. For blast #1, the maximum horizontal and vertical

554   PGA were equal to 1.2g and 1.3g, while for blast #2 the values were 0.8g and 3.6g, respectively. In

555   both cases, the blast-induced ground motion attenuated rapidly with distance and reached values

556   smaller than 0.01g at about 180 m distance. The PGV values provide an exponentially decreasing

557   trend with distance, consistent with other field test evidences (e.g. Gianella and Stuedlein, 2017;

558   Amoroso et al., 2017), recording ranges from 0.14 to 0.0007 m/s at 20 and 250 m distance from the

559   blast centers, respectively.

560

561   **5.3. Post-blast investigations and comparison to all previous data**

562   Fig. 11 shows the comparisons between the average profiles of q_t, K_D and V_S acquired in the pre-

563   and post-blast investigation campaigns, for both panels. Error bars are displayed in order to take

564   into account the variability of measurements within the different soil units.

565
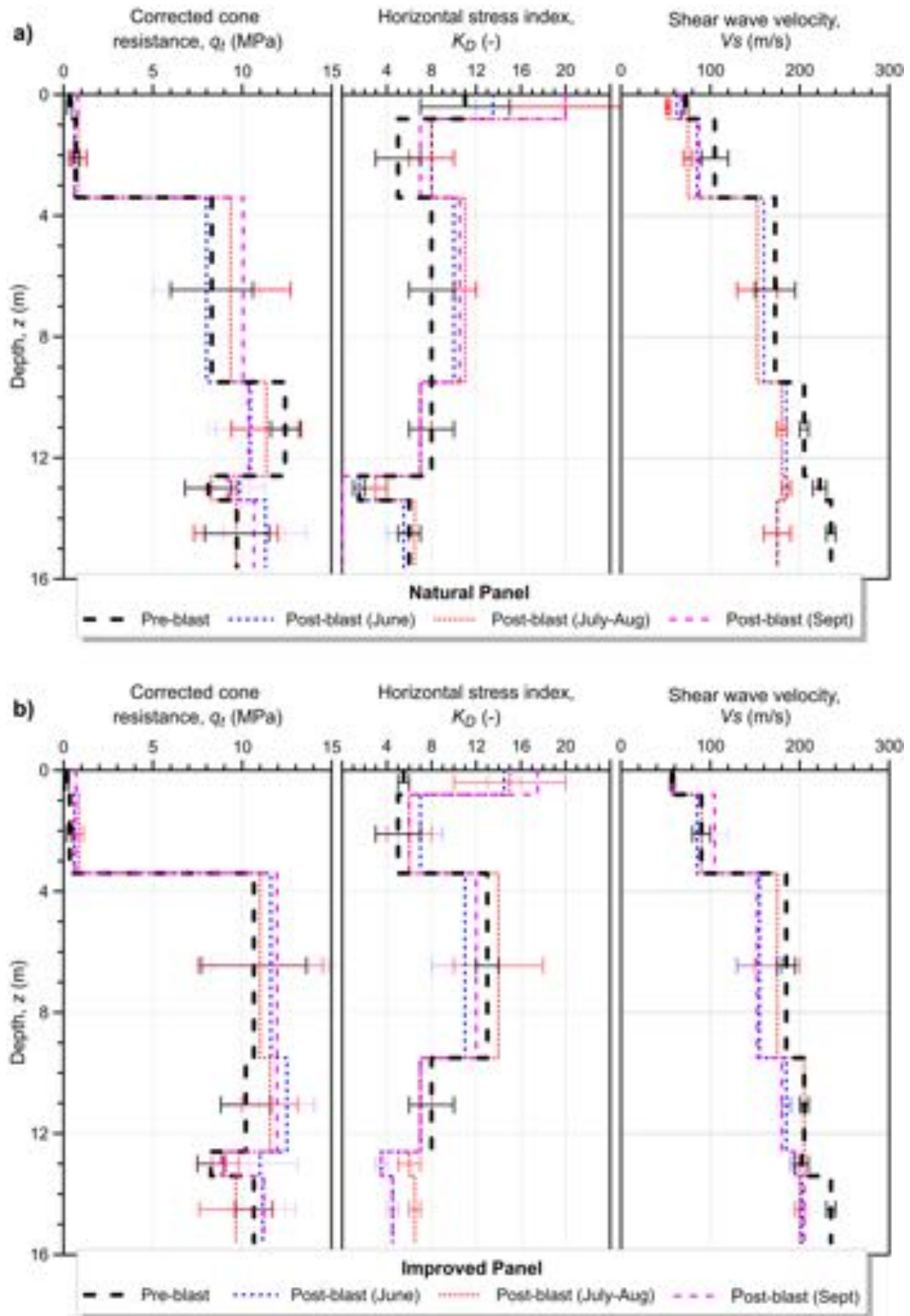
Fig. 11. Variation of the geotechnical and geophysical parameters before and after the blast test, obtained from CPTU and SDMT in the NP (a) and the IP (b).

With reference to the IP after blasting, the comparison of the piezocone results reveals a general slight increase of the corrected cone resistance in the silty sands (SM), although the ranges reported in Fig. 11b do not appear to differ significantly. Negligible changes in the q_t profiles can be appreciated within the lower sands/silty sands. Similarly, the cone resistance profiles in the liquefied layer (3.4-9.5 m) of the NP (Fig. 11a) slightly increase with time (from June to July-August to September-October), whilst the underlying layers do not show any significant change, probably as a consequence of the charge locations. It is worth observing that the horizontal spatial variability of the subsoil complicates at time the direct comparison of the different CPTU soundings.

Based on the DMT results, a few days after blasting, the horizontal stress index turned out to maintain approximately its average value within the liquefiable layer of the IP (Fig. 11b), confirming the effectiveness of the piers in silty sand deposits. On the other hand, a small increase is detectable for the same unit in NP (Fig. 11a), consistently with CPTU measurements, probably due to some densification induced by the blast-liquefaction settlements. The bottom layers do not show any substantial increase. In later investigation campaigns, i.e. both in July-August and in September-October, K_D values stabilized in both the blast areas, showing on average a significant increase only within the liquefiable layer in the IP.

Finally, post-blasting time-dependent stiffness changes cannot be clearly identified in the IP (Fig. 11b), while an overall small V_S decrease is observed in the NP (Fig. 11a). This last finding agrees, for example, with the results obtained by Mahvelati et al. (2016) in Pleistocene-aged sandy deposits, whereas differs from the observations made by Passeri et al. (2018) in Holocene-aged silty sands of Mirabello trial site (Emilia-Romagna, Italy). However, the Mirabello deposits are relatively new Holocene sands in comparison to the deposits of the present study area. Therefore, differences in geologic age and soil fabric may explain the differences in the rate and magnitude of stiffness changes.

593   In Fig. 12, the main results of the geoelectric surveys executed in the different time intervals in

594   correspondence of the IP along the profile PS (see Figs. 2a, 2b, 2e, and 2f) are reported to a reliable

595   investigation depth of 7 m. The measured resistivity data generally depict a very low resistivity

596   environment (on average within 4 to 9 Ohm.m, Fig. 12a), even after the RAP construction (Fig.

597   12b). This is related both to the clayey and silty sand formations at the site and to the relevant

598   saturating water conductivity. Indeed, water samples collected in wells located in the area (Fig. 1)

599   revealed anomalously high electrical conductivity values (more than 1200 μS/cm). This condition,

600   together with the low confining pressures due to pier installation near the ground surface, has

601   influenced the imaged resistivity data, partially compromising the ability of the surveys in detecting

602   resistivity changes related to the blast effects. Particularly, inverted resistivity data were not always

603   able to image significant resistivity variations in the subsurface, particularly in the NP, contrary to

604   previous literature examples (e.g. Passeri et al., 2018). For this reason, raw apparent resistivity data

605   are presented only in the IP, since these data better reflect the local resistivity variations,

606   particularly in correspondence with the RAP columns.
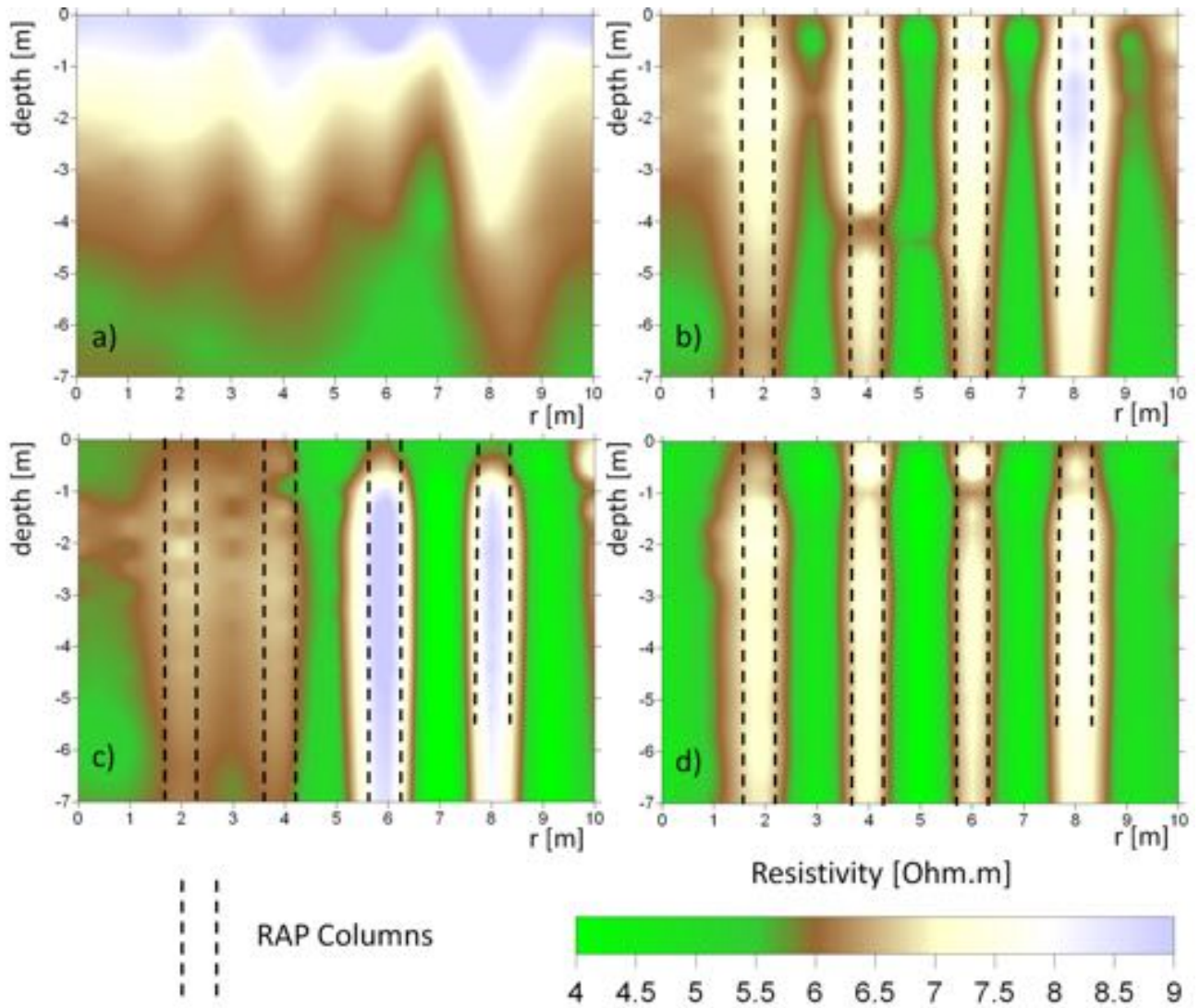
Fig. 12. Apparent resistivity data imaged along the profile PS in correspondence of the IP in the different time windows of the surveys: natural soil (a); treated soil before blast (b); treated soil after blast – June (c); treated soil after blast – September (d).

Indeed in the IP the comparison of resistivity distribution imaged before and after the RAP installation (Figs. 12a and 12b) satisfactorily defines the subsoil modifications related to the installation of the gravel columns (black dashed lines in Figs. 12b, 12c and 12d). The four RAPs intercepted by the survey line are indeed well depicted in the resistivity section showing a relatively higher resistivity with respect to the natural soil. The last column of the section is known to be driven only to 5.5 m depth. Nevertheless, apparent resistivity data also show a partial increase in resistivity at greater depths probably due to compaction of the subsoil following tamping. The first

two piers along the section appear instead to be less homogeneous, as independently confirmed by quality control tests performed during their construction (Fig. 12b). After the blast testing the same first two piers along the section show a more significant resistivity reduction (Fig. 12c), which makes them less evident with respect to the surrounding soil. This effect could be related to increased water pressure in this zone of the IP and to partial column modifications after the blast which could have compromised RAP column resistance, given also their initial reduced stiffness. In this same zone of the IP, increased settlements after the blast have been depicted (Fig. 8) corroborating the geophysical evidence. Nevertheless, the apparent RAP column modifications do not appear to be permanent because the columns are again correctly imaged in the resistivity section acquired four months after the blast (Fig. 12d). Notwithstanding the difficult environment in terms of resistivity distribution, the geophysical surveys proved effective in imaging the variations induced by the blast tests within the RAP columns and can be suggested as a potential monitoring system.

Three trenches were excavated in the N350°-N355° direction (TR1a-c-d in Fig. 13a) and one in the transverse N65° direction (TR1b in Fig. 13a). The geometrical arrangement of the trenches made it possible to obtain detailed information on the sand boil genesis and on the previous fractures/conduits used by the liquefied sands in the 2012 earthquake. Particularly, the main sand boils developed during the blast tests shown in Fig. 6c reached the surface through the pore pressure transducer hole (PPT5, Figs. 13b and 13c). Evidence of liquefied sand ejected toward the surface was also found along the external part of the profilometer (CNP, Fig. 13d). This sand was also observed filling a sub-horizontal fracture marking a stratigraphic contact (yellow flags in Fig. 13b) between a silty clay, with sparse pebbles and a few charcoals (stratigraphic level 1 in Fig. 13b), and an oxidized silty clay (stratigraphic level 2 in Figs. 13b and 13c). Evidence from the 2012 liquefaction (Figs. 13e and 13f) was also found in a 8 cm thick sand layer with a sharp basal contact on the vegetated surface at the time of the earthquake (Figs. 13e and 13f). The 2012 liquefied sand utilized an almost vertical thin fracture, visible to a depth of 1.5 m to reach the surface (Fig. 13g). A

light grey clayey silt layer at the bottom of the trench (stratigraphic level 3 in Fig. 13c) was also

observed, and provisionally recognized as one of the impermeable deposits over the liquefiable

sand. The ejection of sand during the blast test largely utilized pre-existing artificial paths (PPT5

and CNP) and the weak stratigraphic contact between level 1 and 2.

Fig. 13. Geometrical arrangement of the trenches (a); details of the most significant features

exposed in the walls. Sand boils from the blast test (b) were generated by sand moving upward

using the PPT5 pore pressure transducer, colored flags in (c), and the external part of the CNP

profilometer (d) as conduits. Sand from CNP moved sub-horizontally, as shown by yellow flags, in

(b). The white dashed circle in (f) indicates the remnants of the vegetation at the ground surface,

covered by the 2012 sand blow (bottom of the blow marked by colored flags in e, f). Details of the

2012 vertical path (colored flags) developed along a thin fracture in (g).

6. Conclusions

Full-scale blast-induced liquefaction tests (Bondeno, Italy) made it possible to evaluate the effectiveness of Rammed Aggregate Pier® (RAP) treatment in mitigating liquefaction hazards in silty sands. A multidisciplinary approach was used to increase the understanding obtained from the inter-related methods used to document blast-induced liquefaction behavior. The tests were performed on treated and untreated panels at a test site where sand boils indicated liquefaction during the 2012 M_w 6.1 Emilia-Romagna earthquake.

The controlled blasting experiment induced liquefaction in the natural panel (NP) consisting of untreated silty sands (FC ≈ 15-45%) and produced surface settlements of 7 to 10 cm. Numerous sand boils were induced and volumetric strains within the liquefied layers were similar to those that would be expected from earthquake-induced liquefaction, in agreement with previous blast experiments. Grain size distribution curves of the induced sand boils confirmed a selective loss of fines relative to the source beds in-situ (paleochannel of the Po River), in agreement with previous blast experiments and earthquake events. In-hole accelerometers were able to record maximum peak accelerations equal to 45g and 52g, and further analysis will be performed to estimate the blast-induced shear stress and shear strain.

Within the improved panel (IP), excess pore pressure ratios were lower than in the untreated panel, but still greater than 75%. Despite these relatively high R_u values, the measured settlements (20 to 50 mm) were significantly lower than in the untreated natural panel, as confirmed by topographical surveys and geotechnical monitoring. In addition, sand boil formation was strongly reduced. Therefore, RAP treatment resulted in reducing liquefaction-induced settlements to acceptable levels for many structures in comparison with the untreated natural soil. The site investigations performed after blasting also confirmed that the treated soil maintains approximately its pre-blast geotechnical properties, while the natural untreated soil developed lower values that later recovered with time. After blasting, some temporary RAP modifications were also detected by the electrical resistivity profiles and topographical surveys in correspondence with the piers that showed lower stiffness during the construction procedure.

685 Further in-depth data analysis is necessary to understand the fundamental mechanisms leading to

686 the reduction in settlement within the treated panel that may be related to soil densification,

687 increased lateral stress, and composite soil-column behavior during reconsolidation.

688

References

Adalier, K., Elgamal, A., 2004. Mitigation of liquefaction and associated ground deformations by stone columns. Engineering Geology 72: 275-291.

Adalier, K., Elgamal, A., Meneses, J., Baez, J.I., 2003. Stone columns as liquefaction contermeasure in non-plastic silty soils. Soil Dynamics and Earthquake Engineering 23: 571-584.

Alexander, G., Arefi, J., Geoffrey, R.M., 2017. Performance of a stone column foundation system subjected to severe earthquake shaking. Proceedings of the 3rd International Conference on Performance-based Design in Earthquake Geotechnical Engineering - PBD-III, Vancouver, Canada.

Amoroso, S., Milana, G., Rollins, K.M., Comina, C., Minarelli, L., Manuel, M.R., Monaco, P., Franceschini, M., Anzidei, M., Lusvardi, C., Cantore, L., Carpena, A., Casadei, S., Cinti, F.R., Civico,R., Cox, B.R., De Martini, P.M, Di Giulio, G., Di Naccio, D., Di Stefano, G., Facciorusso, J., Famiani, D., Fiorelli, F., Fontana, D., Foti, S., Madiai, C., Marangoni, V., Marchetti, D., Marchetti, S.L., Martelli, L., Mariotti, M., Muscolino, E., Pancaldi, D., Pantosti, D., Passeri, F., Pesci, A., Romeo, G., Sapia, V., Smedile, A., Stefani, M., Tarabusi, G., Teza, G., Vassallo, M., Villani, F., 2017. The first Italian blast-induced liquefaction test (Mirabello, Emilia-Romagna, Italy): description of the experiment and preliminary results. Annals of Geophysics 60(5), S0556. https://doi.org/10.4401/ag-7415.

Amoroso, S., Rollins, K.M., Monaco, P., Holtrigter, M., Thorp, A., 2018. Monitoring ground improvement using the seismic dilatometer in Christchurch, New Zealand. Geotechnical Testing Journal 41(5), 946-966. https://doi.org/10.1520/GTJ20170376.

737 Amoroso, S., Rollins, K.M., Andersen, P., Gottardi, G., Tonni, L., García Martínez, M.F.,

738 Wissmann, K., Minarelli, L., 2019. Full-scale testing of liquefaction mitigation using rammed

739 aggregate piers in silty sands. Proceedings of the 7th International Conference on Eartquake

740 Geotechnical Engineering – 7 ICEGE, Rome, Italy, 656-663.

741 Amoroso, S., Comina, C., Marchetti, D., 2020. Combined P- and S-wave measurements by seismic

742 dilatometer test (SPDMT): a case history in Bondeno (Emilia Romagna, Italy). Geotechnical

743 Testing Journal 43(2). https://doi.org/10.1520/GTJ20180233.

744 Ashford, S., Rollins, K.M., Lane, J., 2004. Blast-induced liquefaction for full-scale foundation

745 testing. Journal of Geotechnical and Geoenvironmental Engineering 130(8), 798-806.

746 ASTM D2487-11, 2011. Standard practice for classification of soils for engineering purposes

747 (Unified Soil Classification System). West Conshohocken, PA: ASTM International.

748 Caputo, R., Poli, M.E., Minarelli, L., Rapti, D., Sboras, S., Stefani, M., Zanferrari, A., 2016.

749 Palaeoseismological evidence for the 1570 Ferrara earthquake, Italy. Tectonics 35(6), 1423-1445.

750 Civico, R., Brunori C.A., De Martini P.M., Pucci S., Cinti F.R., Pantosti D., 2015. Liquefaction

751 susceptibility assessment in fluvial plains using airborne LIDAR: the case of the 2012 Emilia

752 earthquake sequence area (Italy). Natural Hazards and Earth System Sciences 15, 2473–2483.

753 Cubrinovski, M., Bray, J.D., de la Torre, C., Olsen, M., Bradley, B., Chiaro, G., Stocks, E.,

754 Wotherspoon, L., Krall, T., 2018. Liquefaction-induced damage and CPT characterization of the

755 reclamations at CentrePort, Wellington. Bulletin of the Seismological Society of America, 108(3B),

756 1695–1708. DOI: 10.1785/0120170246.

757 De Martini, P.M., Cinti, F.R., Cucci, L., Smedile, A., Pinzi, S., Brunori, C.A., Molisso, F., 2012.

758 Sand volcanoes induced by the April 6th 2009 Mw 6.3 L'Aquila earthquake: a case study from the

759 Fossa area, Italian Journal of Geosciences 131, 410-422.

760 Emergeo Working Group, 2013. Liquefaction phenomena associated with the Emilia earthquake

761 sequence of May-June 2012 (Northern Italy). Natural Hazards and Earth System Sciences 13(4),

762 935-947.

Finno, R.J., Gallant, A.P., Sabatini, P.J., 2016. Evaluating ground improvement after blast densification at the Oakridge landfill. Journal of Geotechnical and Geoenvironmental Engineering 142(1), 04015054.

Fontana, D., Lugli, S., Marchetti Dori, S., Caputo, R., Stefani, M., 2015. Sedimentology and composition of sands injected during the seismic crisis of May 2012 (Emilia, Italy): clues for source layer identification and liquefaction regime. Sedimentary Geology 325, 158-167.

Fontana, D., Amoroso, S., Minarelli, L., Stefani, M., 2019. Sand liquefaction phenomena induced by a blast test: new insights from composition and texture of sands (late Quaternary, Emilia, Italy). Journal of Sedimentary Research 89(1),13-27, https://doi.org/10.2110/jsr.2019.1.

Gianella, T.N., Stuedlein, A., 2017. Performance of Driven Displacement Pile–Improved Ground in Controlled Blasting Field Tests. Journal of Geotechnical and Geoenvironmental Engineering 143(9), 04017047.

Giona Bucci, M., Villamor, P., Almond, P., Tuttle, M., Stringer, M., Ries, W., Smith, C., Hodge, M., Watson, M., 2018. Associations between sediment architecture and liquefaction susceptibility in fluvial settings: The 2010–2011 Canterbury Earthquake Sequence, New Zealand. Engineering Geology 237, 181-197.

Green, R.A., Olgon, C.J., Wissmann, K.J., 2008. Shear stress redistribution as a mechanism to mitigate the risk of liquefaction. Proceedings of the 4th Geotechnical Earthquake Engineering and Soil Dynamics Conference: Liquefaction Triggering, Consequences, and Mitigation, Sacramento, California, GSP 181.

Harada, K., Orense, R.P., Ishihara, K., Mukai, J., 2010. Lateral stress effects on liquefaction resistance correlations. Bulletin of the New Zealand Society for Earthquake Engineering 43(1), 13-23.

Hwang, S., Roberts, J.N., Stokoe, K.H. II, Cox, B.R., van Ballegooy, S., Soutar, C., 2017. Utilizing direct-push crosshole seismic testing to verify the effectiveness of shallow ground improvements: a

case study involving low-mobility grout columns in Christchurch, New Zealand, Proceedings of Grouting 2017, Honolulu, Hawaii, 415-424.

Jamiolkowski, M., Lo Presti D.C.F., Manassero, M., 2003. Evaluation of relative density and shear strength of sands from cone penetration test and flat dilatometer test. Proceedings of Soil Behaviour and Soft Ground Construction, GSP 119, 201-238.

Li, H., Liu, S., Tong, L., Xu, X., 2018. Investigating the resonant compaction effect on laterally loaded piles in layered soil. Engineering Geology 246: 1-11.

Luzi, L., Pacor, F., Ameri, G., Puglia, R., Burrato, P., Massa, M., Augliera, P., Franceschina, G., Lovati, S., Castro, R., 2013. Overview on the strong-motion data recorded during the May–June 2012 Emilia seismic sequence. Seismological Research Letters 84(4), 629-644.

Mahvelati, S., Coe, J.T., Stuedlein, A.W., Asabere, P., Gianella, T.N., 2016. Time-rate variation of the shear wave velocity (site stiffness) following blast- induced liquefaction. Proceedings of Proceedings of GeoChicago, Chicago, Illinois, 904–913.

Marchetti, D., Monaco, P., Amoroso, S., Minarelli, L., 2019. In situ tests by Medusa DMT. Proceedings of the XVII European Conference on Soil Mechanics and Geotechnical Engineering ECSMGE-2019, Reykiavik, Iceland, DOI: 10.32075/17ECSMGE-2019-0657.

Maurer, B.W., Green, R.A., Wotherspoon, L.M., Bastin, S., 2019. The stratigraphy of compound sand blows at sites of recurrent liquefaction: implications for paleoseismicity studies. Earthquake Spectra, 35(3), 1–20. DOI: 10.1193/041818EQS097M.

Minarelli, L., Amoroso, S., Tarabusi, G., Stefani, M., Pulelli, G., 2016. Down-hole geophysical characterization of middle-upper Quaternary sequences in the Apennine Foredeep, Mirabello, Italy, Annals of Geophysics 59(5), S0543. https://doi.org/10.4401/ag-7114.

Mitchell, J.K., 2008. Mitigation of liquefaction potential in silty sands. Proceedings of From Research to Practice in Geotechnical Engineering Congress 2008, 433-451.

Mitchell, J.K., Solymar, Z.V., 1984. Time-dependent strength gain in freshly deposited or densified sand, Journal of Geotechnical Engineering 110(11), 1559-1576.

814 Mitchell, J. K., Wentz, F. L., 1991. Performance of improved ground during the Loma Preita

815 earthquake. Report No. UCB/EERC-91/12, University of California, Berkeley, CA.

816 Narin van Court, W.A., Mitchell, J.K., 1994. Soil improvement by blasting, Journal of Explosives

817 Engineering 12(3): 34-41.

818 Molinari, I., Argnani, A., Morelli, A., Basini, P., 2015. Development and testing of a 3D seismic

819 velocity model of the Po plain sedimentary basin, Italy. Bulletin of the Seismological Society of

820 America 105(2A), 753-764.

821 Obermeier, S.F., 1998. Liquefaction evidence for strong earthquakes of Holocene and latest

822 Pleistocene ages in the states of Indiana and Illinois, USA. Engineering Geology 50: 227-254.

823 Papathanassiou, G., Mantovani, A., Tarabusi, G., Rapti, D., Caputo, R., 2015. Assessment of

824 liquefaction potential for two liquefaction prone areas considering the May 20, 2012 Emilia (Italy)

825 earthquake. Engineering Geology 189, 1-16.

826 Passeri, F., Comina, C., Marangoni, V., Foti, S., Amoroso, S., 2018. Geophysical tests to monitor

827 blast-induced liquefaction, the Mirabello (NE, Italy) test site. Journal of Environmental and

828 Engineering Geophysics 23(3): 319-333, DOI: 10.2113/JEEG23.3.319.

829 Pesci, A., Amoroso, S., Teza, G., Minarelli, L., 2018. Characterisation of soil deformation due to

830 blast-induced liquefaction by UAV-based photogrammetry and terrestrial laser scanning.

831 International Journal of Remote Sensing and Remote Sensing Letters 39(22), 8317–8336.

832 https://doi.org/10.1080/01431161.2018.1484960.

833 Pondrelli, S., Salimbeni, S., Perfetti, P., Danecek, P., 2012. Quick regional centroid moment tensor

834 solutions for the Emilia 2012 (northern Italy) seismic sequence. Annals of Geophysics 55(4), 615–

835 621. https://doi.org/10.4401/ag-6146.

836 Rayamajhi, D., Nguyen, T.V., Ashford, S.A., Boulanger, R.W., Lu, J., Elgamal, A., Shao, L., 2014.

837 Numerical study of shear stress distribution for discrete columns in liquefiable soils. Journal of

838 Geotechnical and Geoenvironmental Engineering 140(3), 04013034.

Rayamajhi, D., Ashford, S.A., Boulanger, R.W., Elgamal, A., 2016. Dense granular columns in liquefiable ground. I: shear reinforcement and cyclic stress ratio reduction. Journal of Geotechnical and Geoenvironmental Engineering 142(7), 04016023.

Robertson, P.K., Wride, C.E., 1998. Evaluating cyclic liquefaction potential using the cone penetration test. Canadian Geotechnical Journal 35(3): 442-459.

Rollins, K.M., Lane, J.D., Nicholson, P.G., Rollins, R.E., 2004. Liquefaction hazard assessment using controlled blasting techniques, Proceedings of 11th International Conference on Soil Dynamics and Earthquake Engineering, Berkeley, California, 2: 630 - 637.

Saftner, D.A., Green, R.A., Hryciw, R.D., 2015. Use of explosives to investigate liquefaction resistance of aged sand deposits. Engineering Geology 199, 140-147.

Saftner, D.A., Zheng, J., Green, R.A., Hryciw, R., Wissmann, K., 2018. Rammed aggregate pier installation effect on soil properties. Institution of Civil Engineers-Ground Improvement 171(2), 63-73.

Salgado, R., Boulanger, R.W., Mitchell, J.K., 1997. Lateral stress effect on CPT liquefaction resistance correlations. Journal of Geotechnical and Geoenvironmental Engineering 123(8), 726-735.

Smith, M.E., Wissmann, K., 2018. Ground improvement reinforcement mechanisms determined for the Mw 7.8 Muisne, Ecuador, earthquake. Proceedings of the 5th Geotechnical Earthquake Engineering and Soil Dynamics Conference: Liquefaction Triggering, Consequences, and Mitigation - GEESDV 2018, Austin, Texas, GSP 290, 286-294.

Stefani, S., Minarelli, L., Fontana, A., Hajdas, I., 2018. Regional deformation of Late Quaternary fluvial sediments in the Apennines foreland basin (Emilia, Italy), International Journal of Earth Sciences, 107(7), 2433–2447. DOI:10.1007/s00531-018-1606-x.

Tonni, L., Gottardi, G., Amoroso, S., Bardotti, R., Bonzi, L., Chiaradonna, A., d'Onofrio, A., Fioravante, V., Ghinelli, A., Giretti, D., Lanzo, G., Madiai, C., Marchi, M., Martelli, L., Monaco, P., Porcino, D., Razzano, R., Rosselli, S., Severi, P., Silvestri, F., Simeoni, L., Vannucchi, G.,

Aversa, S., 2015. Interpreting the deformation phenomena triggered by the 2012 Emilia seismic sequence on the Canale Diversivo di Burana banks, Rivista Italiana di Geotecnica 49(2), 28-38. http://www.associazionegeotecnica.it/sites/default/files/rig/2_2015_028ton.pdf

Toscani, G., Burrato, P., Di Bucci, D., Seno, S., Valensise, G., 2009. Plio-Quaternary tectonic evolution of the northern Apennines thrust fronts (Bologna-Ferrara section, Italy): seismotectonic implications. Italian Journal of Geosciences, 128, 605-613.

Vautherin, E., Lambert, C., Barry-Macaulay, D., Smith, M., 2017. Performance of rammed aggregate piers as a soil densification method in sandy and silty soils: experience from the Christchurch rebuild, Proceedings of the 3rd International Conference on Performance-based Design in Earthquake Geotechnical Engineering - PBD-III, Vancouver, Canada.

Wentz, F.J., van Ballegooy, S., Rollins, K.M., Ashford, S.A., Olsen, M.J., 2015. Large scale testing of shallow ground improvements using blast-induced liquefaction, Proceedings of the 6th International Conference on Earthquake Geotechnical Engineering - 6ICEGE, Christchurch, New Zealand.

Wissmann, K.J., van Ballegooy, S., Metcalfe, B.C., Dismuke, J.N., Anderson, C.K., 2015. Rammed aggregate pier ground improvement as liquefaction method in sandy and silty soils. Proceedings of the 6th International Conference on Earthquake Geotechnical Engineering - 6ICEGE, Christchurch, New Zealand.

Wotherspoon, L.M., Cox, B.R., Stokoe, K.H. II, Ashfield, D.J., Phillips, R.A., 2015. Utilizing direct-push crosshole testing to assess the effectiveness of soil stiffening caused by installation of stone columns and rammed aggregate piers, Proceedings of the 6th International Conference on Earthquake Geotechnical Engineering - 6ICEGE, Christchurch, New Zealand.

Zhang, G., Robertson, P.K., Brachman, R.W.I., 2002. Estimating liquefaction-induced ground settlements from CPT for level ground. Canadian Geotechnical Journal, 39: 1168-1180. DOI: 10.1139/T02-047